國立成功大學
物理學系所

碩士學位論文

用 STAR 探測器在 $\sqrt{s_{NN}}$ = 200 GeV 的金離子與金離子對撞實驗中利用雙渺子末態量測 ϒ 粒子的生成抑制現象

Measurements of the ϒ suppression in Au-Au collisions at $\sqrt{s_{NN}}$ = 200 GeV via the dimuon decay channel at the STAR experiment

研 究 生：張哲嘉

學　　號：L26061155

指導教授：楊毅教授

中華民國一零九年七月二十七日

國立成功大學

碩士論文

用 STAR 探測器在 $\sqrt{s}$ = 200 GeV 的金離子金離子對撞實驗中利用雙渺子末態量測 Υ 粒子的生成抑制現象

Measurement of the Υ suppression in Au-Au collision at $\sqrt{s}$ = 200GeV via the dimuon decay channel at the STAR experiment

研究生：張哲嘉

本論文業經審查及口試合格特此證明

論文考試委員：

指導教授：

系(所)主管：

物理系 系主任 羅光耀

中　華　民　國　109　年　7　月　27　日

摘　要

位於美國布魯克海文國家實驗室 (Brookhaven National Laboratory) 的相對論性重離子對撞機 (Relativistic Heavy Ion Collider) 中的 STAR 實驗於 2014 年完成了渺子探測器 (Muon Telescope Detector) 的安裝，使我們能夠藉由雙渺子衰變來研究夸克偶對 (quarkonium) 相關的物理。

在這篇論文中，我們結合了於 2014 及 2016 年收集的質心能量為 200 GeV 的金離子金離子對撞實驗數據，藉由測量核抑制因子 (nuclear modification factor, R_{AA}) 來研究 Υ 粒子在金離子金離子對撞實驗中受到夸克膠子電漿態 (quark gluon plasma) 影響而產生的生成抑制現象。

關鍵字：STAR, MTD, quarkonium, Υ, R_{AA}

Abstract

The Solenoid Tracker At RHIC (STAR) is one of the most important high energy nuclear physics experiments in the world and the only on-going experiment at Relativistic Heavy Ion Collider, which is located at Brookhaven National Laboratory. The Muon Telescope Detector (MTD) is dedicated for identifying and triggering muons at STAR and it was installed in 2014. This allows us to study physics using muon final states.

In this thesis, we used the data of Au-Au collision at $\sqrt{s_{NN}}$ = 200 GeV which is collected in 2014 and 2016 to study the suppression effect for Υ(1, 2, 3S) due to the quark gluon plasma (QGP) created in heavy-ion collisions by measuring the Υ nuclear modification factor (R_{AA}).

Keywords: STAR, MTD, quarkonium, Υ, R_{AA}

Acknowledgements

I would like to express my deepest thanks to my adviser Prof. Yi Yang first of all. I learned not only the knowledge of high energy physics but also the techniques of analysis from him. I would like to thank Prof. Zhangbu Xu, the former spokesperson of the STAR experiment for providing us an opportunity of visiting BNL. The opportunity of visiting BNL gave me lots of valuable experiences and let me meet many good friends.

Next, I would like to thank Prof. Lijuan Ruan, the current spokesperson of STAR, for all the help and encouragement. Many thanks to Dr. Rongrong Ma, Dr. Shuai Yang, and Mr. Pengfei Wang for lots of supports and suggestions for my Υ study. Especially thanks to Mr. Pengfei Wang not only the supports for my research but also sharing with me much useful information about python, pyROOT, and mac. I also want to thank Zhen Wang for many interesting ideas for programming.

Lots of thanks to Te-Chuan for teaching me ROOT and many correct concepts of programming, and also for teaching me cooking and driving as we were in BNL. Thanks to Han-Sheng Li shared life experiences and many interesting things to me. Feng-Han Chang and Pu-kai Wang also gave many help and great suggestions on my analysis. Thanks to Chan-jui for the discussions of our analysis. They help me a lot.

Thanks to Chen-Wei Lee and Rogers Pan for taking exercise such as jogging and boxing with me during this stressed period. Thanks to Hao Huang, Hsiang-Chieh Hsu, Yu-Ming Liu, Nina Chen, Chiun Fu, Chun-Wei Su, and many friends in NCKU High Energy Physics group. I really had a great time in this group with you.

I would like to thank my girlfriend, Yin-Hsuan Wu for spiritual support and encouragement. I'm very lucky to meet you during studying for my master's degree. Finally, I would like to thank my parents. I am very appreciative of the unselfish financial and spiritual support.

Contents

List of Tables

List of Figures

Chapter 1 Introduction

Particle physics (high energy physics) involves the most fundamental components of the material. In 2012, Higgs boson was discovered by ATLAS [12] and CMS [7] in the Large Hadron Collider at CERN. This means that we have discovered all the particles predicted by the Standard Model of particle physics (SM). Some people may think that there is nothing new in particle physics, but the truth is there are still a lot of questions that can not be answered. For example, why the observed antimatters are very rare compared to the matters in this universe? Is there a single theory that can describe all these fundamental interactions, such as electromagnetic, weak, strong, and gravitational interactions? Why there are three generations of quarks and leptons? What are the dark matter and dark energy? These questions are so interesting that deserved us to work hard and discover the answers.

Physicists and cosmologists believe that this universe was started with the Big Bang [13] which an extremely hot and dense state as known as the Quark Gluon Plasma (QGP) state. Physicists believe that there are a very short time and small place where the environment is very similar to the state right after the Big Bang right after heavy-ion collisions. The Solenoid Tracker At RHIC (STAR) is an important high-energy nuclear physics experiment at the Relativistic Heavy Ion Collider (RHIC) which is located at Brookhaven National Laboratory (BNL) in New York. The main goal of STAR is to study the formation and characteristics of the QGP state. The results from RHIC and LHC indicate that there is a strong suppression on the quarkonium production in QGP and we can quantify this suppression by measuring the nuclear modification factor (R_{AA}) which will be defined later.

I arranged my thesis as follows. In Chapter 2, I will present the theoretical overview of the SM of particle physic as well as QGP and the Υ mesons. In Chapter 3, I will give a brief introduction to the STAR experiment. Chapter 4 discusses the data set and the event selections in the analysis. Chapter 5 presents the analysis of the measurement of Υ R_{AA} in Au-Au collision at $\sqrt{s_{NN}}$ = 200 GeV in the STAR experiment. Finally, the conclusions are given in Chapter 6.

Chapter 2 Theoretical overview

2.1 The Standard Model of particle physics

Using a single theory to describe all the four fundamental interactions has been a dream for physicists for a long time. The four fundamental interactions are strong, electromagnetic, weak, and gravitational interactions. The Standard Model of particle physics (SM) describes the interactions except for gravitation between particles. There are two categories for the particles in SM which are fermions and bosons and they have half-integer spin and integer spin, respectively. The summary of the elementary particles is shown in Fig. 2.1.

There are two categories for the fermions – quarks and leptons. And there are three generations for the fermions and each generation includes two quarks and two leptons. Except for the mass difference, all the properties are the same between different generations. The fermions in the first generation compose the matters in the universe and follow the Fermi-Dirac statistics and the Pauli exclusion principle. For fermions, all of them, charged leptons and neutrinos are able to participate the electromagnetic interaction. Due to the special properties of Quantum Chromodynamics (QCD), quarks are able to be observed in the confined bound states. The leptons don't experience strong interactions because they don't have the color charge.

The interactions of the SM can be described in the gauge theory. The U(1) and the SU(2) local gauge symmetries are able to describe the electromagnetic and the weak interactions, respectively. And the strong interaction can be described by the SU(3) [14].

Bosons in SM are gluon, photon, $W^{\pm}$, Z^0 and Higgs bosons and they are following the Bose-Einstein statistics. The force carriers for the strong and electromagnetic interactions are the gluon and photon, respectively [14]. The $W^{\pm}$ and Z^0 bonson are the force carriers of the weak interactions [14]. Higgs mechanism [15] provided a way to obtain masses for the fundamental particles and the exsisted state of the Higgs field is the Higgs boson.

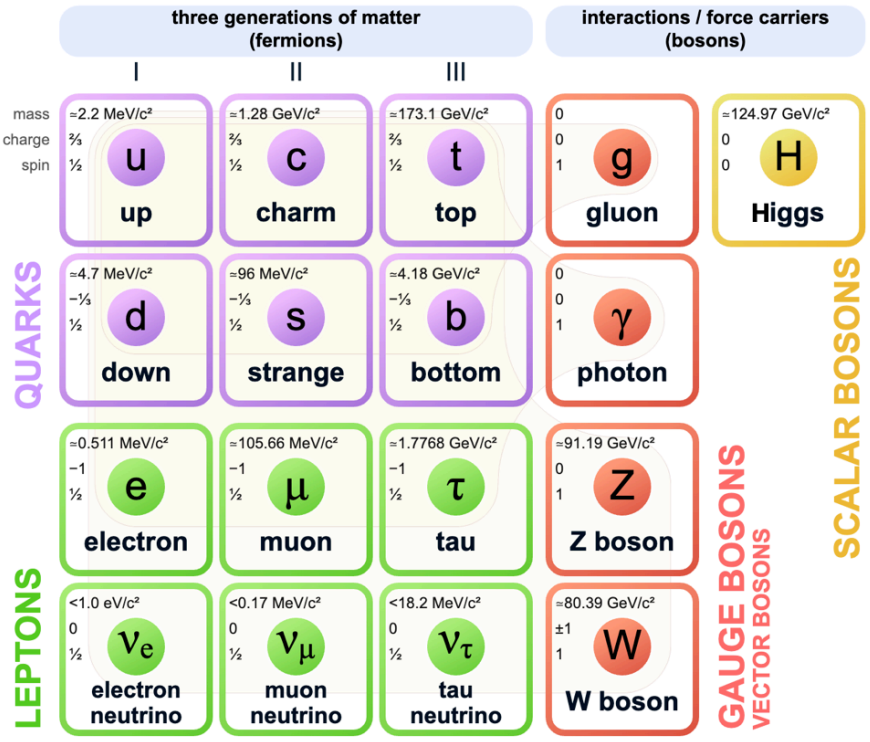

Figure 2.1: The elementary particles in SM. [1]

2.2 The ϒ mesons

The quarks in the confined bound states are called hadrons. There are two categories for the hadrons – baryons and mesons. Baryons are composed of three quarks, for instance proton and neutron. On the other hand, mesons are composed of a quark and an anti-quark. The confined bound states of quark and its anti-quark are quarkonium state. The quarkonia of charm and anti-charm quarks are called charmonium ($c\bar{c}$), for example, J/ψ and $\psi(2S)$. And the ϒ mesons are the bottomoniums ($b\bar{b}$), the quarkonium of bottom, and anti-bottom quarks.

The ϒ mesons were first discovered by the team led by L. M. Lederman at Fermilab in 1977 [16]. The ϒ(1S) meson was the first particle containing the bottom quark to be discovered and its mass is about 9.46 GeV. The masses of the excited ϒ states, ϒ(2S) and ϒ(3S), are about 10.02 and 10.36 GeV. The summary of the bottomonium family is shown in Fig. 2.2.

In order to describe the production of quarkonia, there are several models, such as Color

Singlet Model (CSM), Color Evaporation Model (CEM), Color Octet Mechanism (COM) and Color Glass Condensate (CGC) model. The details of these models can be found in [14, 17, 18]. The production cross sections of Υ(1S), Υ(2S) and Υ(3S) measured by the LHCb in p-p collisions at $\sqrt{s}$ = 7 TeV are shown in Fig. 2.3 [3].

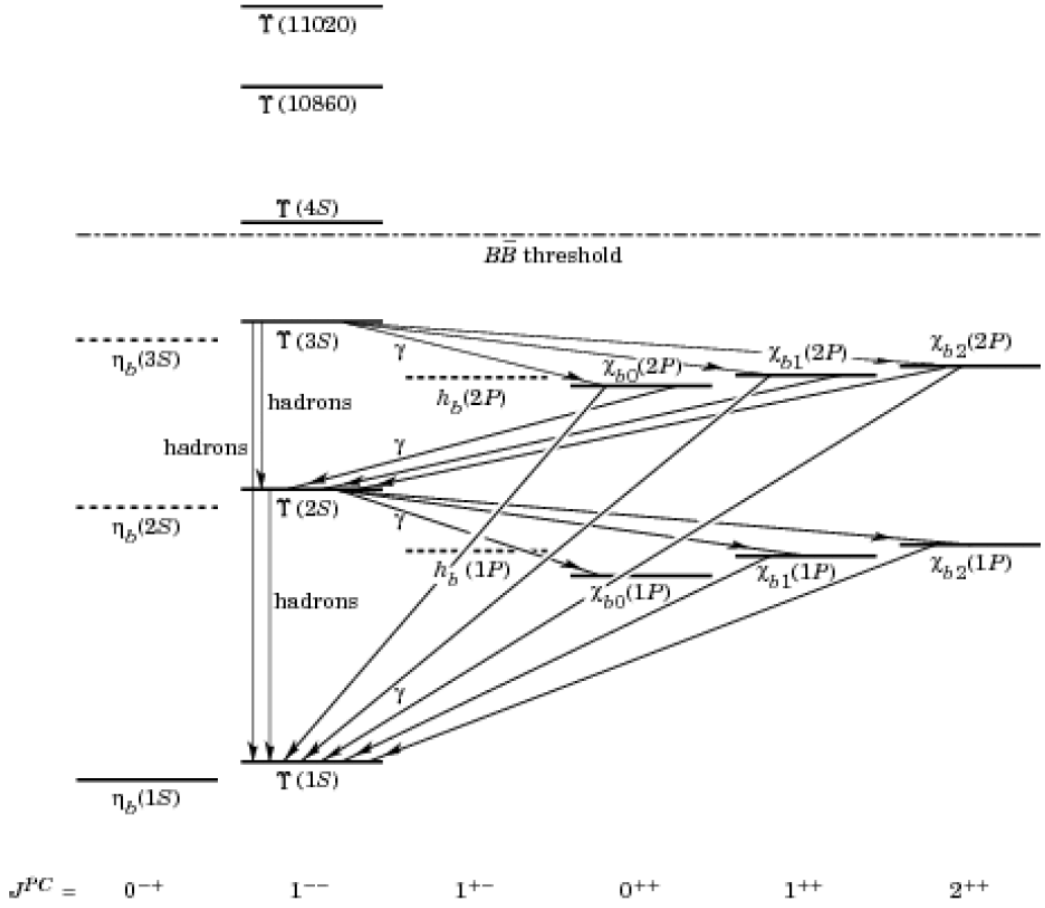

Figure 2.2: The summary of the bottomonium family. [2]

2.3 Quark-Gluon Plasma and Nuclear Modification Factor R_{AA}

Our universe is believed that it expanded from the extremely high temperature and high density initial state base on the Big Bang theory /citebigbang. In this state, the strong interactions are very weak between the quarks and deconfinement of the quarks and the gluons would form a state called Quark-Gluon Plasma (QGP). Studying the QGP would provide

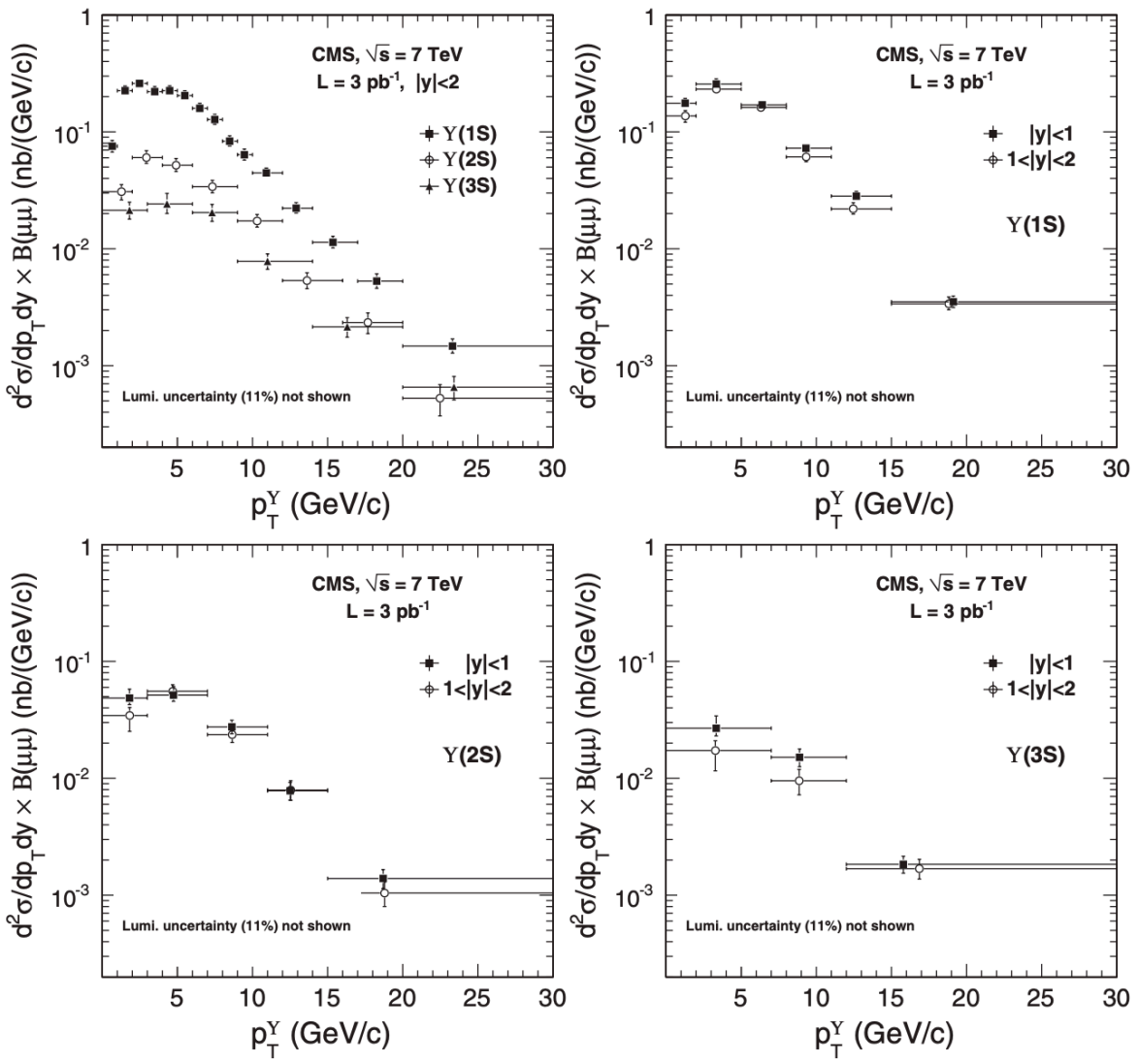

Figure 2.3: The differential cross sections in the rapidity interval |y| < 2 (top left), and in the rapidity intervals |y| < 1 and 1 < |y| < 2 for the ϒ(1S) (top right), ϒ(2S) (bottom left) and ϒ(3S) (bottom right) measured by the CMS in p-p collisions at $\sqrt{s}$ = 7 TeV as a function of ϒ p_T [3].

us valuable information to understanding the evolution of our universe. The phase diagram of the relation between temperature and the chemical potential of the baryon is shown in Fig. 2.4 [4]. According to different models, the boundary of the phase and the critical point would be different. Therefore, the Beam Energy Scan (BES) programs of STAR is dedicated to map the QCD phase diagram and to search the critical point of the first order phase transition.

The production of the quarkonia would be affected by the QGP, such as the suppression and the regeneration of the quarkonium. The suppression of the quarkonium is that the bound states of the quarks and anti-quarks would be destroyed by the color screening effect at extremely high temperatures. The regeneration of the quarkonia is that two free quarks and anti-quarks are very close to each other. Then they form a new state at extremely high densities. This effect would cause the increasing of the number of quarkonia.

Heavy-ion collisions create high temperature and high energy density environment where is the perfect place to study the properties of the QGP. The R_{AA} is defined in Eq. 2.1, where $d^2N_{AA}/dp_T^{\Upsilon}dy$ is the corrected yield of Υ in Au-Au collisions, $d^2\sigma_{pp}/dp_T^{\Upsilon}dy$ is the Υ cross-section in p-p collisions, N_{coll} is the average number of nucleon-nucleon collisions, and $\sigma_{pp}^{inel.}$ is the inelastic cross section in p-p collisions. However, the interpretation of the R_{AA} measurements is complicated since many aforementioned effects are needed to be considered. They can be roughly explained by three scenarios: $R_{AA} = 1$ means the not addition effect in the heavy-ion collisions, $R_{AA} < 1$ means the suppression is dominated in the QGP, and the $R_{AA} > 1$ means the regeneration effect is dominated in QGP. The measurements of the Υ(1S) and the Υ(2S) R_{AA} from CMS and STAR are shown in Fig. 2.5[5].

$$R_{AA} = \frac{\sigma_{pp}^{inel.}}{N_{coll}} \frac{\frac{d^2N_{AA}}{dp_T^{\Upsilon}dy}}{\frac{d^2\sigma_{pp}}{dp_T^{\Upsilon}dy}} \tag{2.1}$$

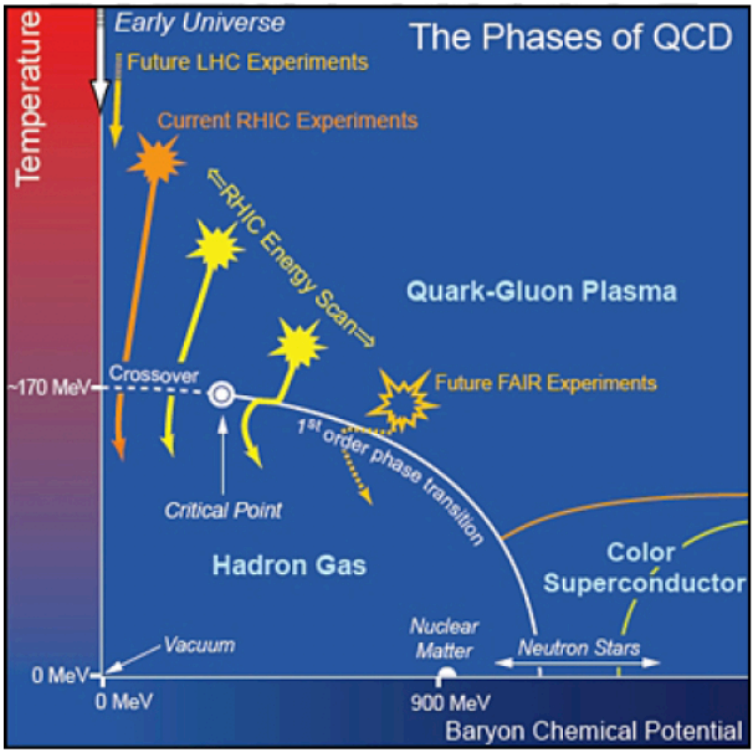

Figure 2.4: The phase diagram of the relation between temperature and the chemical potential of the baryon [4].

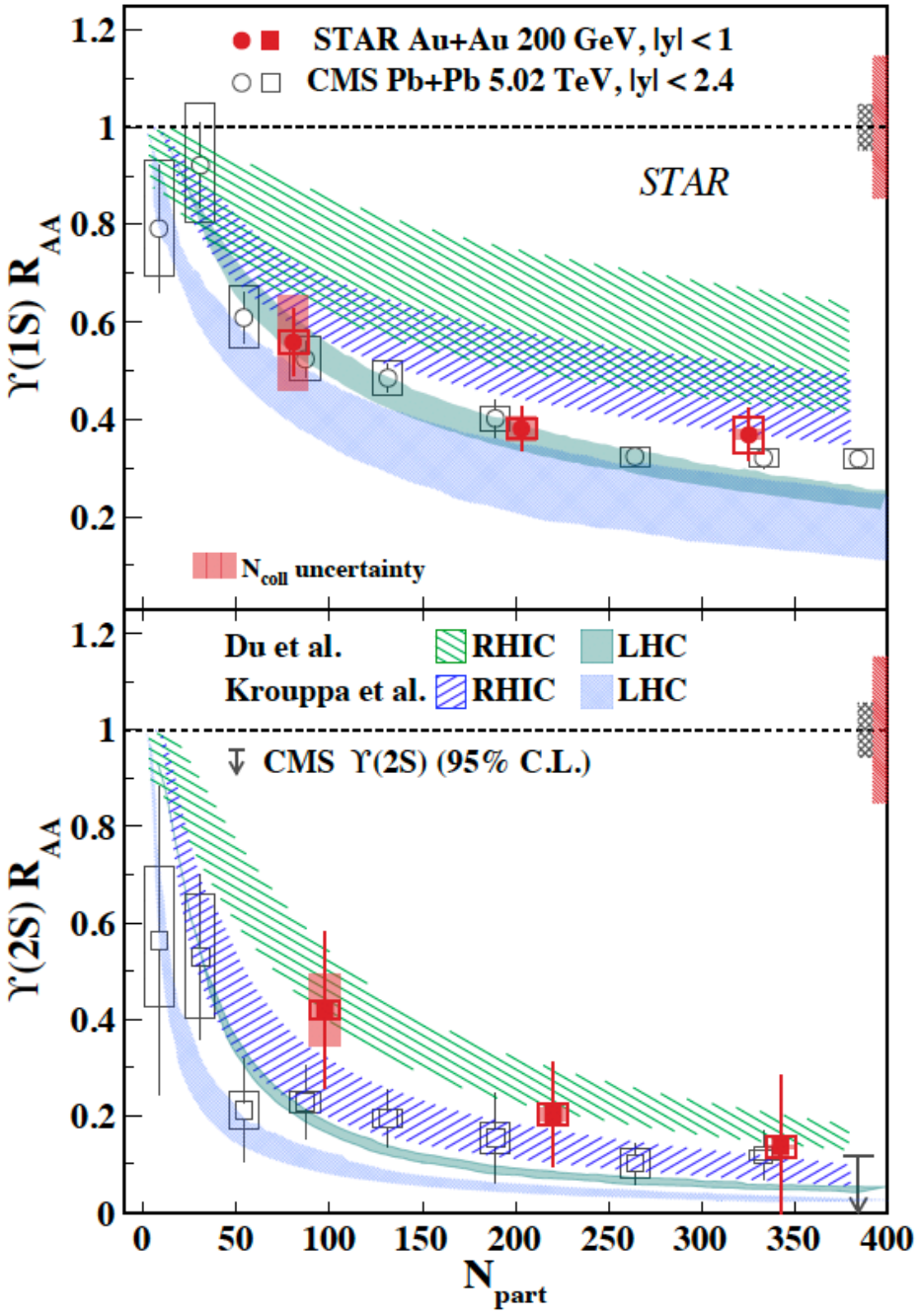

Figure 2.5: The measurements of R_{AA} for Υ(1S) and Υ(2S) from CMS and STAR [5]. The red solid boxes are from STAR [6] and the black open boxes are from CMS [7]

Chapter 3 Experimental apparatus

3.1 Relativistic Heavy Ion Collider (RHIC)

Relativistic Heavy Ion Collider (RHIC) is one of the most versatile colliders in the world, which is located at Brookhaven National Laboratory (BNL) in US. The highest collision energies are 200 GeV and 510 GeV for gold ions (Au-Au) and protons (p-p) collisions, respectively. RHIC is the only collider that has the capability to accelerated and collide the polarized protons in the world. RHIC is composed of the Electron Beam Ion Source (EBIS), Tandem Van de Graaff accelerator, linear accelerator (Linac), Booster Synchrotron, Alternating Gradient Synchrotron (AGS) and AGS-to-RHIC (ATR). Fig. 3.1 shows the layout of the RHIC complex. For heavy ions experiment, the generation of ion beam starts from the Electron Beam Ion Source accelerator, and while for the protons collisions, the Tandem Van de Graaff accelerator plays the role of the proton beam source for RHIC. The beam first accelerates up to 200 MeV in Linac. The Booster Synchrotron serves as an important part by accepting heavy ions from EBIS or protons from Linac and accelerates beams. Then the beams will obtain more energy after injecting to AGS. When the ion beam is accelerated up to the top speed in AGS, it is taken down the AGS-to-RHIC (ATR) transfer line and then inject into the RHIC ring. RHIC started the beam operation since 2000.

3.2 The STAR Experiment

The Solenoid Tracker At RHIC (STAR) is one of the major high-energy nuclear physics experiments in RHIC. It is a general-purpose particle detector with full azimuthal angle coverage ($0 < \phi < 2\pi$), and large pseudorapidity (η) coverage, $-1 < \eta < 1$. The definition of η is $\eta = -\ln[\tan(\frac{\theta}{2})]$, where θ is the angle with respect to beam line.

The STAR detector is composed of several subsystems, such as magnets, Time Projection Chamber (TPC), Vertex Position Detector (VPD), Barrel Electromagnetic Calorimeter (BEMC), Endcap Electromagnetic Calorimeter (EEMC), Time of Flight (ToF), Endcap Time

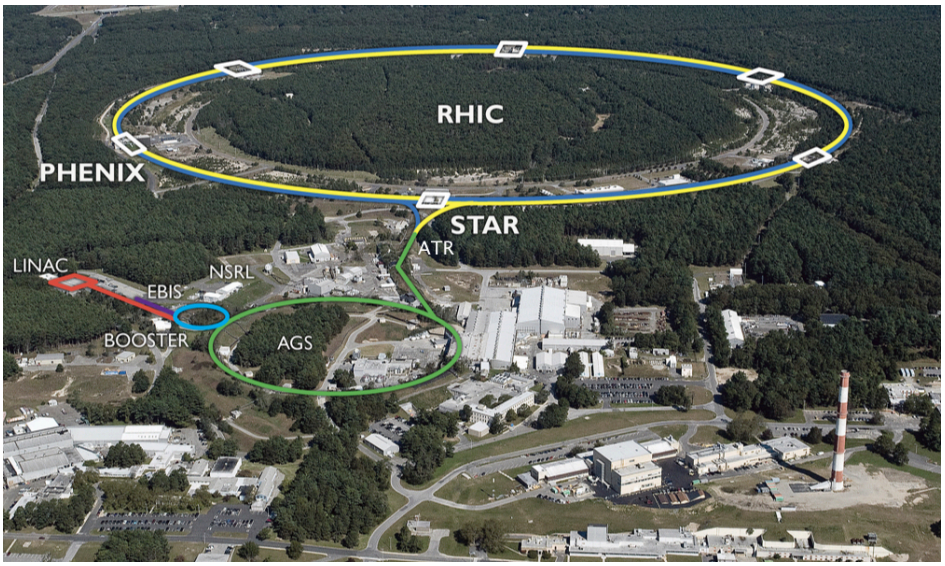

Figure 3.1: The layout of the RHIC complex.

of Flight (EToF) and Muon Telescope Detector (MTD) and so on. The configuration of the STAR detector is shown in Fig. 3.2. The subsystems which are related to this analysis will be described in the following sections.

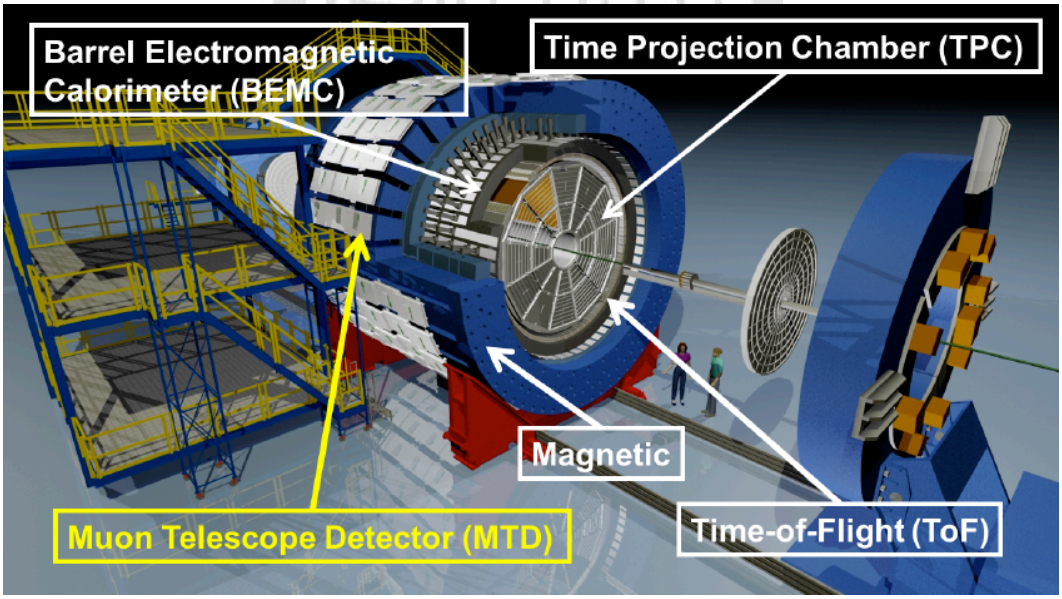

Figure 3.2: The schematics of the STAR detector.

3.3 Magnet System

The main purposes of the magnet system are providing the bending force to charged particle, and this is very powerful for the determination of charge sign and the momentum measurements. The magnet field from 0.25 to 0.5 Tesla parallel to the beamline are provided. Due to the Lorentz force from the magnet field, the particles with different charges would bend in a different direction. The bending curvature of the trajectories of the charged particles is used to measure the momenta. The magnet system is about 6.85 m long. The inner diameter and the outer diameters are about 5.27 m and 7.32 m, respectively. The magnet steels of the magnet system are also used to support the STAR detector.

3.4 Time Projection Chamber (TPC)

The main purpose of TPC is to measure the trajectories of the charged particles and TPC is filled with the P10 gas (10% methane, 90% argon) at 2 mbar above the atmospheric pressure. The trajectories of the charged particles are used to measure the momentums and the charges of particles. The ionization energy losses (dE/dx) of the charged particles are powerful for particle identification due to the different dE/dx distribution of different particles. The energy losses as a function of the particles' momenta for different particles are shown in Fig. 3.3 [8]. However, it works well in low momenta and the energy loss becomes more mass independent in high momentum [8].

The TPC is about 4.2 m long. The inner and outer diameters are about 1m and 4m, respectively. The azimuthal angle coverage is $0 < \phi < 2\pi$ and the pseudorapidity is $|\eta| < 1.8$. Fig. 3.4 shows the structure of the TPC.

3.5 Time-of-Flight (ToF)

The main purpose of ToF is to measure velocities of charged particles using the Multi-gap Resistive Plate Chamber (MRPC) technology. The resistive plates are arranged in par-

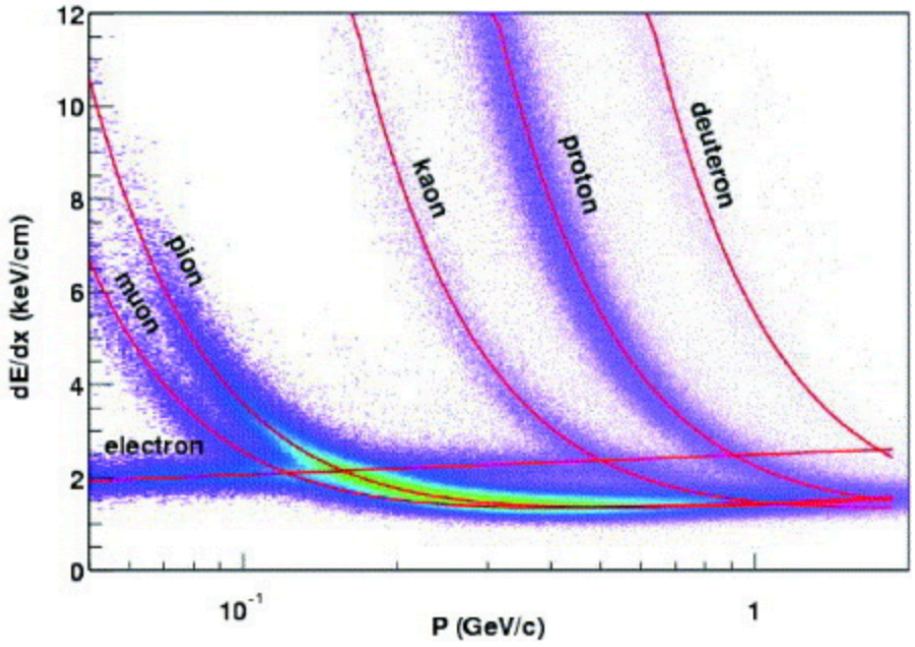

Figure 3.3: The energy losses as a function of momentum for different particles [8].

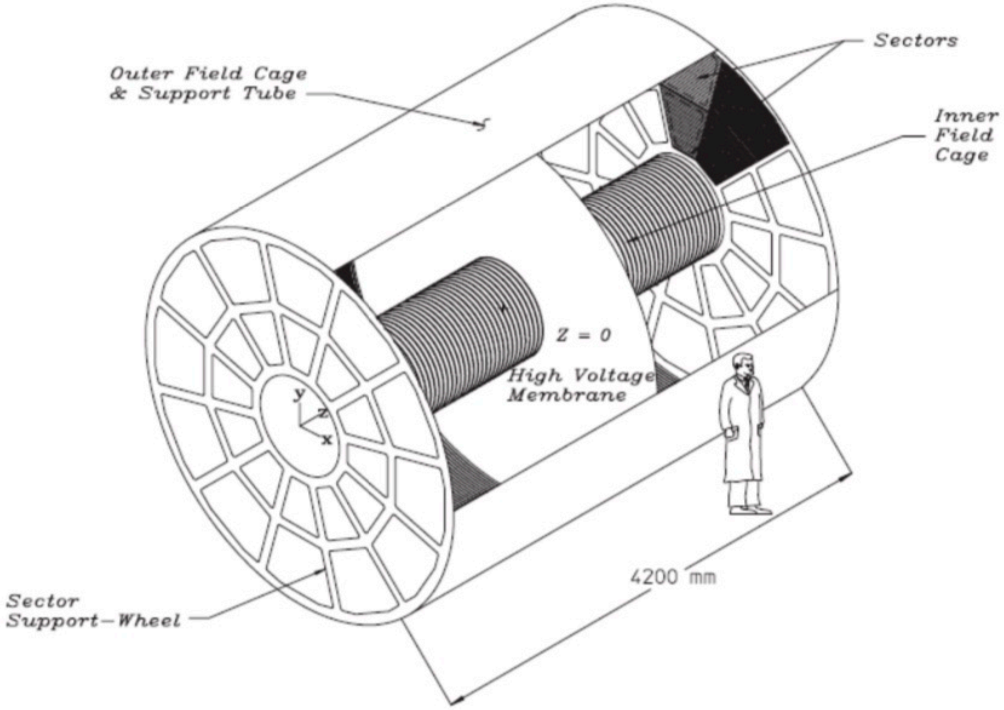

Figure 3.4: The Time Projection Chamber of STAR [8].

allel in the ToF detector. The gas used in the ToF consist of 90% $C_2H_2F_4$, 5% isobutane ($HC(CH_3)_3$) and 5% SF_6.

The time of flight from the ToF and the path length measured by the TPC are used to determined the velocities (β) of charged particles in STAR. The $1/\beta$ is defined as $\frac{1}{\beta} = \sqrt{(\frac{mc}{P})^2 + 1}$, where m and P are particle's mass and momentums, respectively. It is clear that it will be a powerful particle identification variable due to the mass dependence.

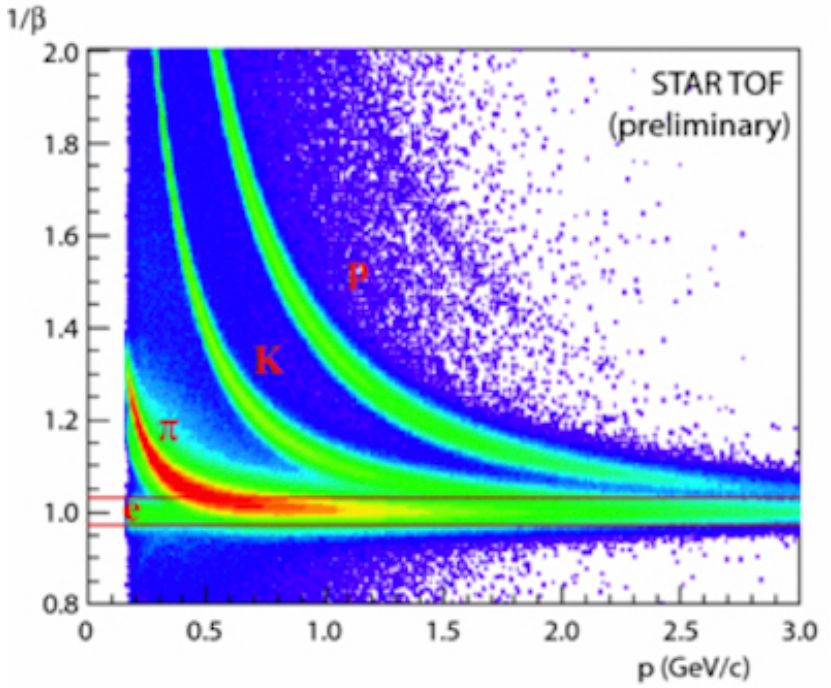

Figure 3.5: The $1/\beta$ as a function of momentum for different charged particles [9].

3.6 Muon Telescope Detector(MTD)

To enhances the muon purity, the MTD modules are installed on the magnetic flux reaction bars (backlegs) which will absorb most of the background hadrons as shown in Fig. 3.6. The schematics of the MTD trays are shown in Fig. 3.7. The MRPC technology described in the previous section is also used in the MTD detector and the gas used in the MTD consist of the 95% $C_2H_2F_4$ and the 5% $HC(CH_3)_3$. The basic informations of the MTD are the radius is about 4 m, the coverage of the pseudo-rapidity is $|\eta| < 0.5$, the coverage of ϕ is about 45 % due to the gas between the backlegs. MTD also plays an important role of triggering muon

related events using the “hits” recorded by MTD when charged particles passing through it. The MTD related triggers are the single muon, electron-muon, and dimuon triggers [10].

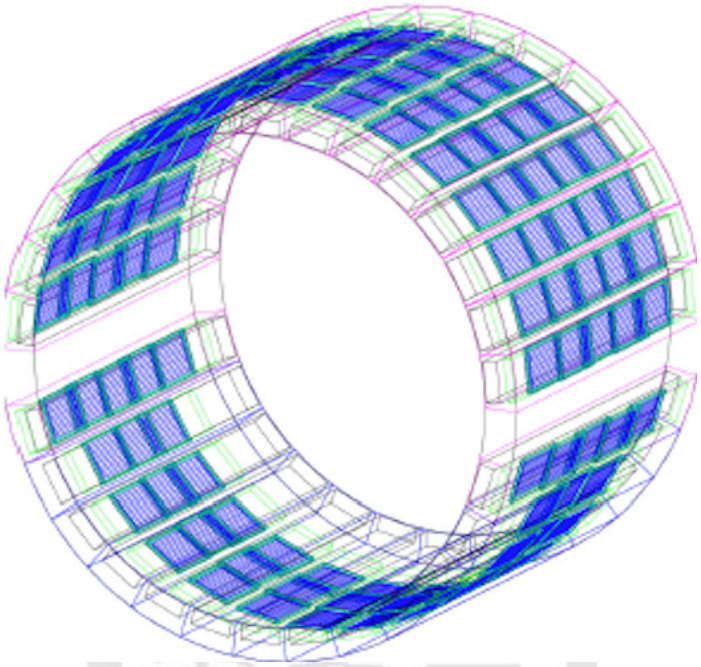

Figure 3.6: The Muon Telescope Detector of the STAR experiment [10].

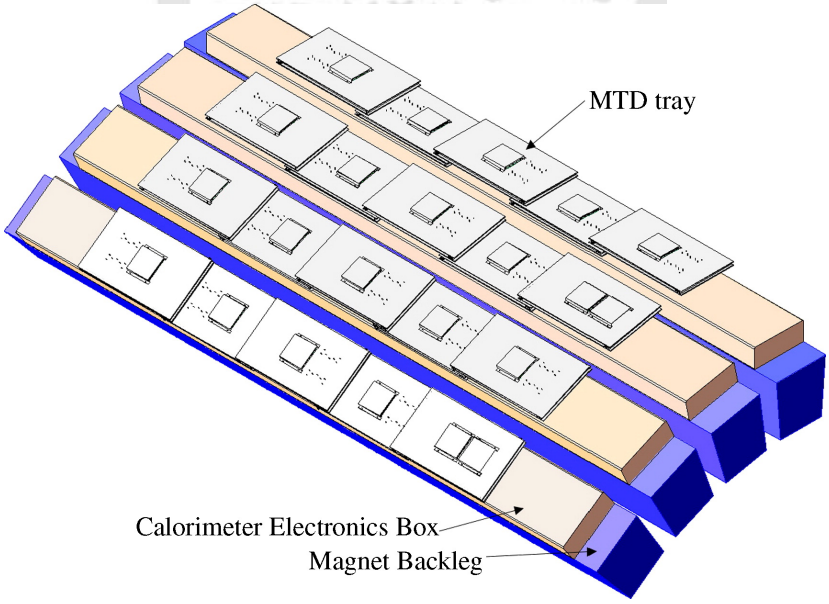

Figure 3.7: The schematics of the MTD trays [10].

Chapter 4 Event selections

4.1 Data sets and basic selections

This analysis used the dimuon triggered events, which requests at least two hits on the MTD detector in each event in the Au-Au collisions data collected in 2014 (Run 14) and 2016 (2016). The corresponding luminosities are 14.2 nb^{-1} and 12.8 nb^{-1} in Run 14 and Run 16, respectively. To ensure data quality, imperfect data due to the detector defects (bad runs) were removed based on the studies done by the BNL group for Run 14 data [11] and the USTC group for Run 16 [5].

Several basic selection criteria are requred to reduce background contamination, such as the tracks associated with the collision vertex (primary tracks) are used; a valid vertex which is located at less than 100 cm of the TPC center along the z-direction; the difference between vertex position by VPD and TPC v_z within 3 cm; the distance of the closest approach (DCA) to the primary vertex should be less than 1.5 cm to suppress secondary decays; the number of the TPC clusters used in reconstruction (NHitsFit) should be greater than 15 (of a maximum of 45) to ensure good momentum resolution; the number of TPC clusters (NHitsDedx) used for dE/dx resolution is required no less than 10 in order to ensure good dE/dx resolution; the ratio of the number of hit points over the number of possible clusters (NHitsRatio) is greater than 0.52 for split-track rejection. The selections of vertex and track quality are summarized in Table 4.1. Additionally, we required each track must match to the MTD hit for the muon candidates selection. To make sure the muon candidates are in the MTD acceptance, we required the transverse momentum (p_T) should greater than 1.3 GeV/c and the absolute value of pseudorapidity (η) should smaller than 0.5.

4.2 Embedding samples

Monte Carlo simulation for $\Upsilon \rightarrow \mu^+\mu^-$ events is needed to calculate the efficiencies and to obtain the shape of the Υ signal. To consider the contribution of background, the simulated

$\|V_z^{TPC}\| < 100$ cm
$\|V_z^{TPC} - V_z^{TPC}\| < 3$ cm
Primary tracks
DCA < 1.5 cm
NHitsFit $\geq$ 15
NHitsDedx $\geq$ 10
NHitsRatio $\geq$ 0.52

Table 4.1: A summary of the selection criteria of vertex and track quality.

signals were "embedded" into the events from real data. The reconstruction procedures in embedding samples are identical to what used in real data. The momentum resolution in embedding samples which is much better than that in the real data must be smeared and this has been done in the Run 14 J/ψ R_{AA} study [11].

4.3 Selection of muon p_T

Due to the limited statistics of the Υ mesons in Run 14 and Run 16, an optional p_T cut is selected by scanning the $\Upsilon \rightarrow \mu^+\mu^-$ signals with different p_T cuts in real data. The additional selections for muon candidates and the signal extraction will be described in Section 4.3.1 and 4.3.2, respectively.

4.3.1 Muon identification: Straight cut method

There are three variables which are related to the MTD hit information (Δy, Δz and ΔToF) and, one variable which is based on the dE/dx information, $n\sigma_\pi$, to be used in the muon identification. Δy and Δz is the difference between the hit position in the MTD and the extrapolated position from the TPC track in the transverse and longitude directions. ΔToF is the difference between the calculated time-of-flight from track extrapolation with the muon particle hypothesis and the measured time-of-flight from MTD. $n\sigma_\pi$ is the normalized

ionization energy loss (dE/dx) which is defined as $n\sigma_{\pi} = \frac{\log(\frac{dE}{dx})_{measured} - \log(\frac{dE}{dx})_{\pi,theory}}{\sigma\log(\frac{dE}{dx})_{measured}}$, where "measured" and "π, theory" represent the measured dE/dx with pion mass hypothesis and the theoretical value for pions, respectively. σ $\log(\frac{dE}{dx})_{measured}$ is the experimental resolution of $\log(\frac{dE}{dx})$ measurements. The summary of the muon identification cuts are shown in Table 4.2.

$\|\Delta y\| < 32$ cm
$\|\Delta z\| < 22$ cm
ΔToF < 0.46 ns
-1 < $n\sigma_{\pi}$ < 3

Table 4.2: The summary of the selection criteria of basic muon identification.

4.3.2 Signal extraction and the selection of muon p_T

Due to the low statistics of the Υ mesons in Run 14 and Run 16 Au-Au data, some additional conditions used in the signal extraction are required, such as the Υ signal shapes from embedding samples; the ratios of $\Upsilon(2S)/\Upsilon(1S)$ and $\Upsilon(3S)/\Upsilon(2S)$ must be constrained within 1 to guarantee the number of the Υ in different excited states are reasonable; the background distributions are obtained from the p_T weighted TPC track pairs, the p_T weights are to correct the difference between the muon p_T distributions for muon candidates and TPC tracks.

To reduced the QCD background, we required the p_T of leading muon is larger than 4 GeV/c and scan different p_T cuts for sub-leading muon to reconstruct Υ. The mass spectra of the Υ candidates in different sub-leading muon p_T selections are shown in Fig. 4.1. The red solid lines are the total fits. The red dashed lines are the background, and the blue, pink, and green area show the Υ(1S), Υ(2S), and the Υ(3S) signal, respectively.

The S/B times the number of total Υ are used to optimize the best muon p_T selection. The distribution of this variable with different subleading muon p_T selection is shown in Fig. 4.2 and the optional cuts for leading and subleading muons are 4 GeV/c and 3 GeV/c, respectively.

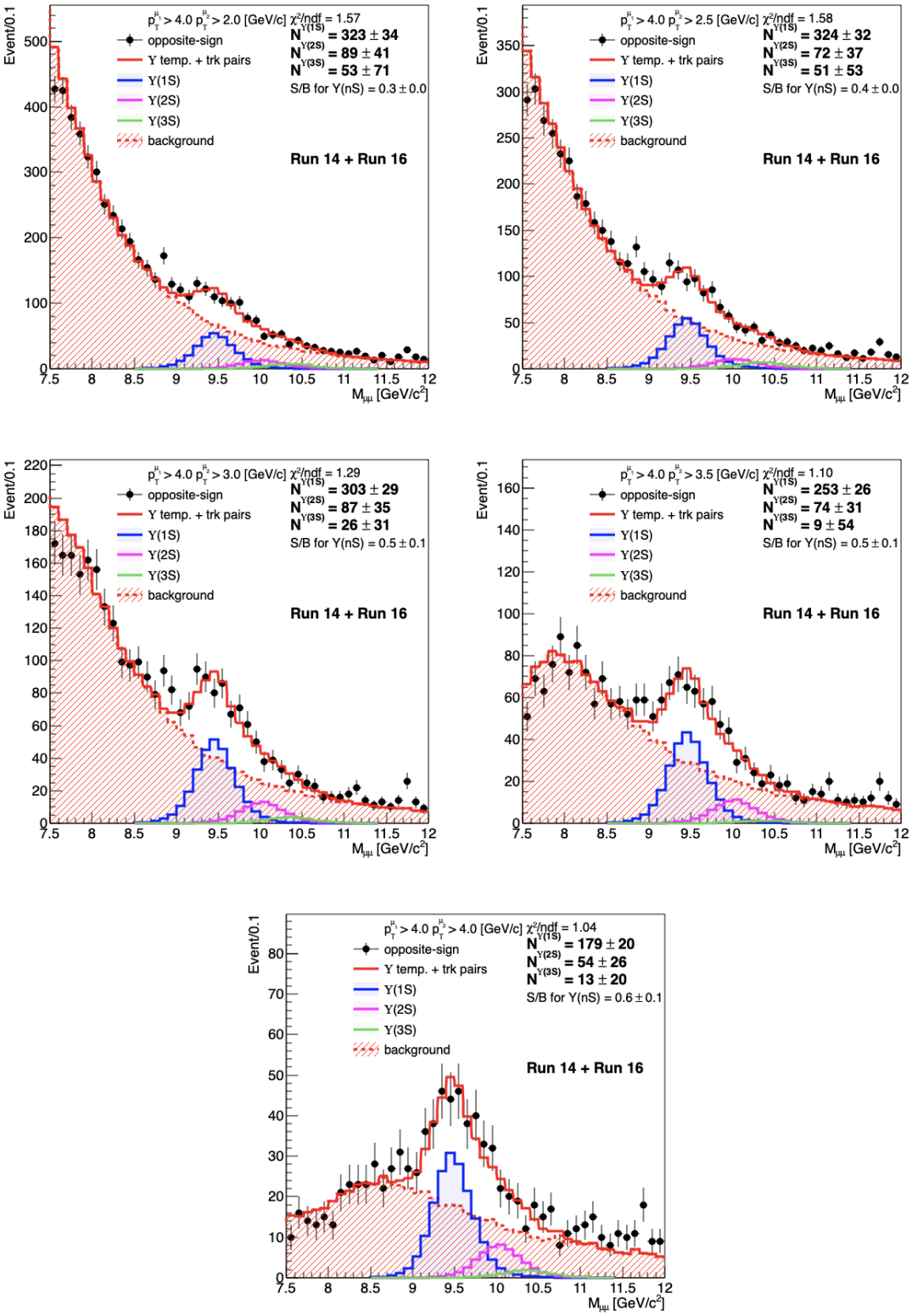

Figure 4.1: Comparison of the mass spectra of Υ candidates in different sub-leading muon p_T selections.

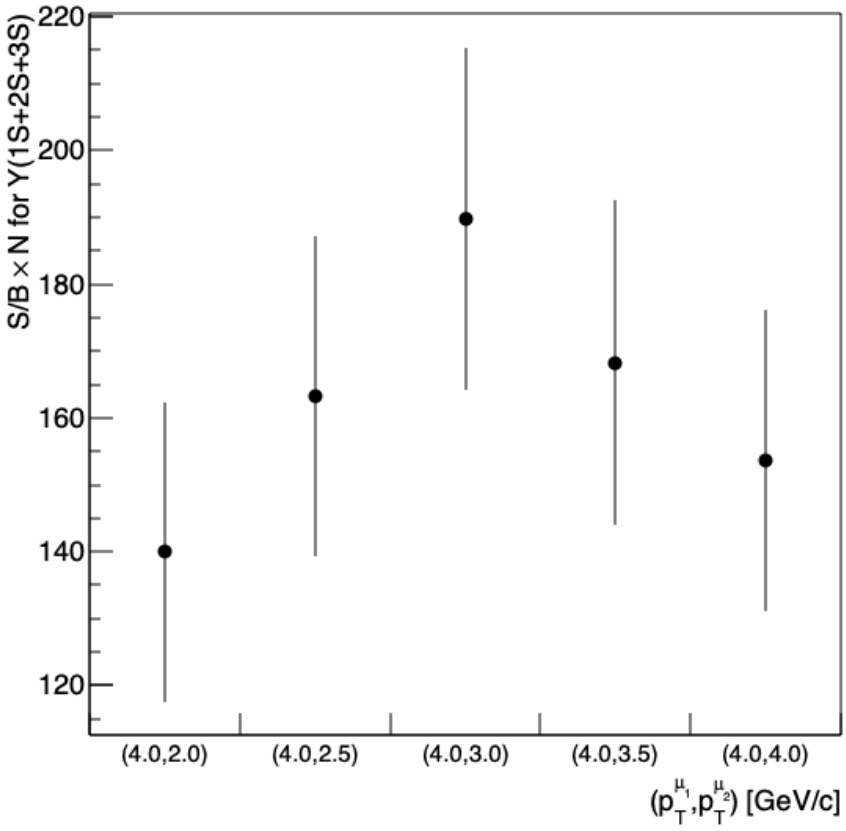

Figure 4.2: Distribution of S/B times the number of total Υ as a function of different p_T selections.

Chapter 5 Measurement of Υ R_{AA}

5.1 Muon identification: Likelihood ratio method

Since the background over signal ratio is large in the Au-Au collisions, an advanced muon identification method, Likelihood Ratio method, is used to reduce the background contamination from background hadrons. The details of this method can be found in [19]. Due to the low statistics of the signal in data, the signal probability density functions (PDFs) are obtained from the embedding samples. There are four variables, $\Delta y \times q$, Δz, $n\sigma_{\pi}$, and DCA are used to build the Likelihood Ratio variable (R). The black solid circles are the opposite-sign (OS) muon candidates subtracted by the same-sign (SS) muon candidates as the signal in data. The red open circles are the distribution of background obtained from SS. The purple histograms are the distributions of the signal from embedding samples (embed.). The PDFs of the muon identification variables are shown in Fig. 5.1. The PDF ratios which used the signal from embedding sample and the background from the SS data are shown in Fig. 5.2. The red solid lines are the bin-to-bin interpolation to evaluate the PDF ratios values of muon candidates.

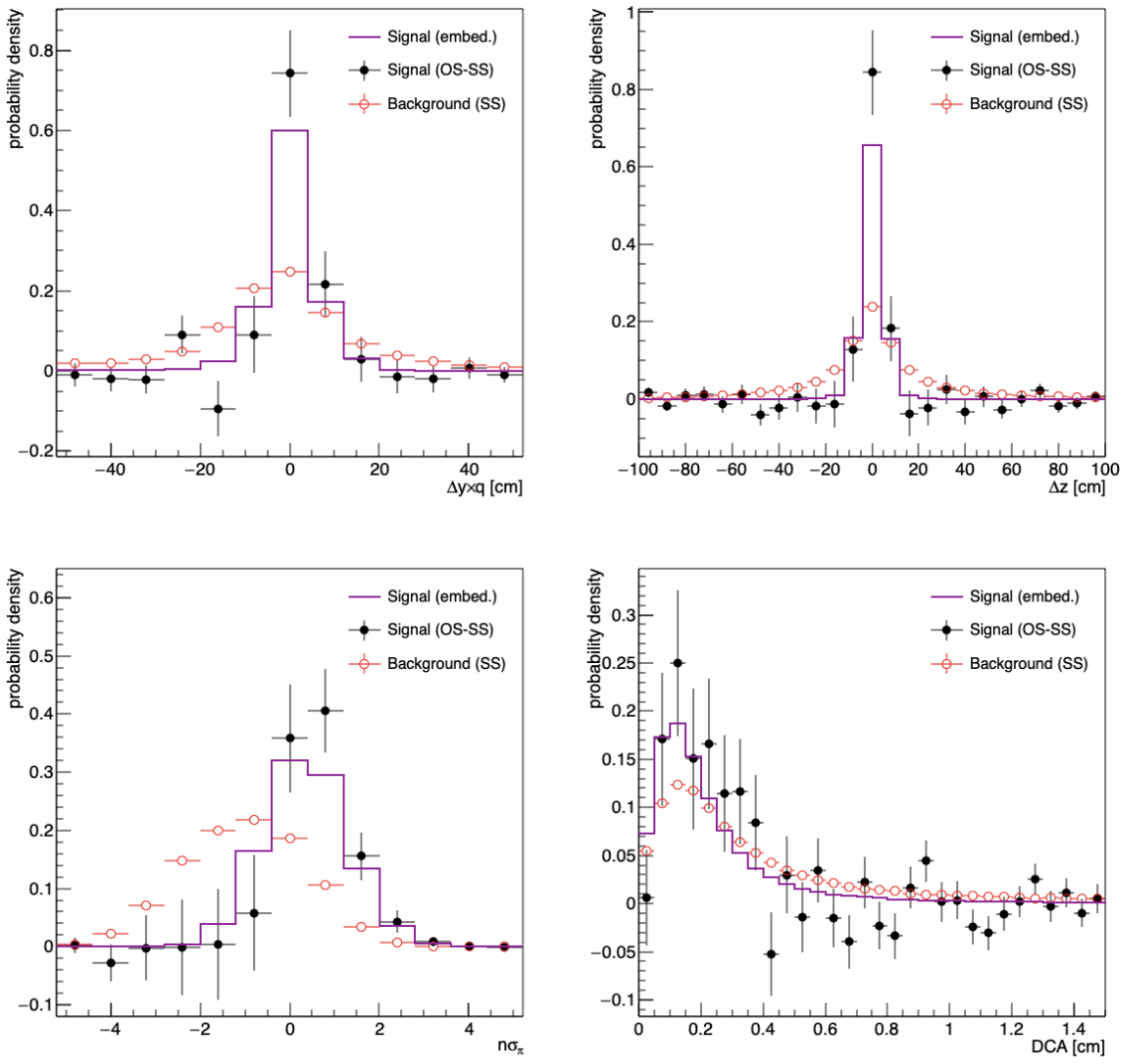

Figure 5.1: The PDFs of the muon identification variables.

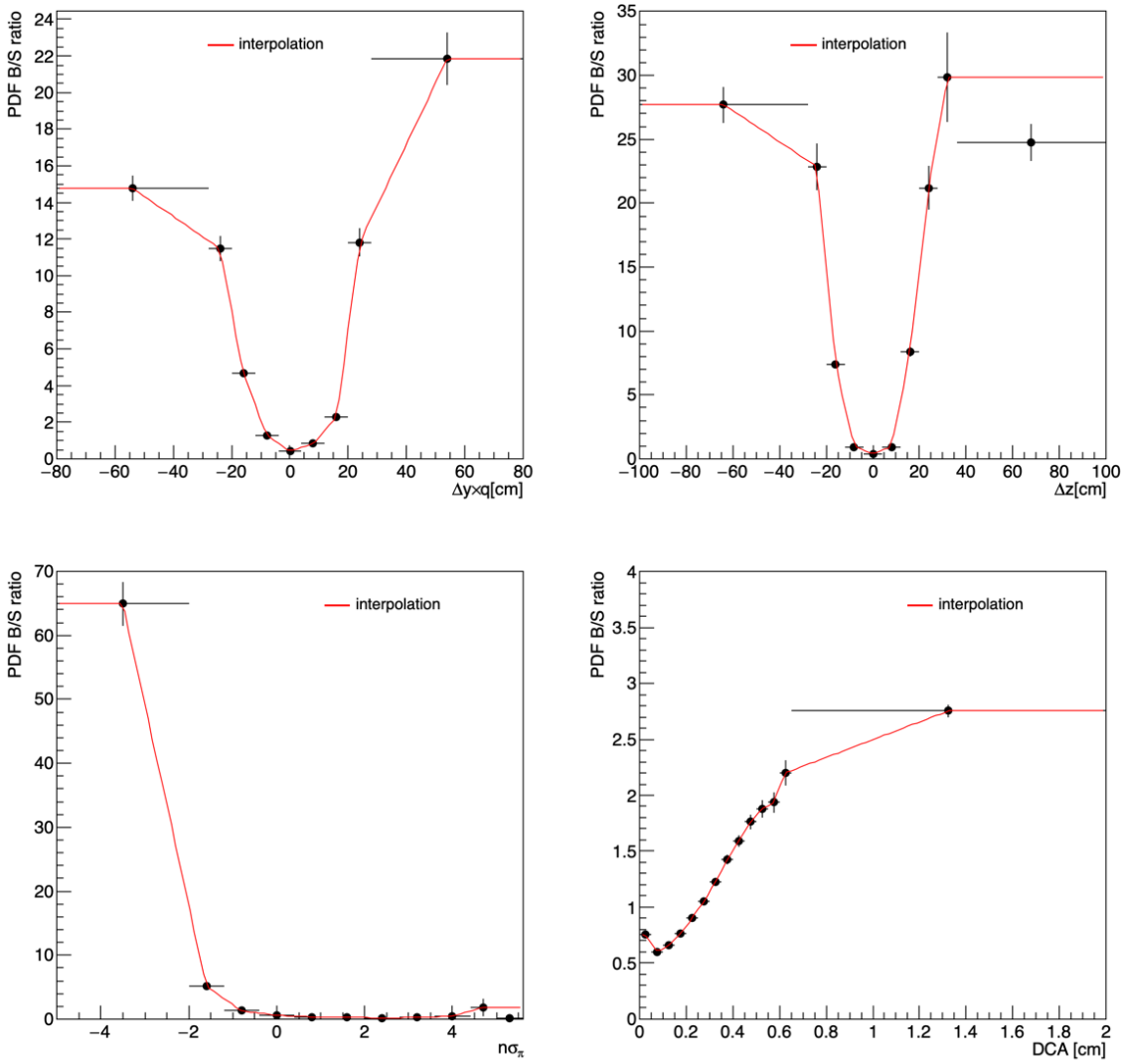

Figure 5.2: The PDF ratios of the muon identification variables.

The R distributions for signal (purple histogram) and background (red histogram) are shown in Fig 5.3. The blue line indicates the best cut which is optimized by the largest value of the background rejection ($1 - \epsilon_B$) times signal efficiency (ϵ_S). Fig. 5.4(a) shows the $(1 - \epsilon_B) \times \epsilon_S$ as a function of R cuts and the red lines indicate the best cut which is R > -0.04 and the corresponding $(1 - \epsilon_B) \times \epsilon_S$. The distribution of $(1 - \epsilon_B)$ vs. ϵ_S is shown in Fig 5.4(b) and the red lines indicate the corresponding $1 - \epsilon_B$ (80%) and ϵ_S (87%) of the best cut.

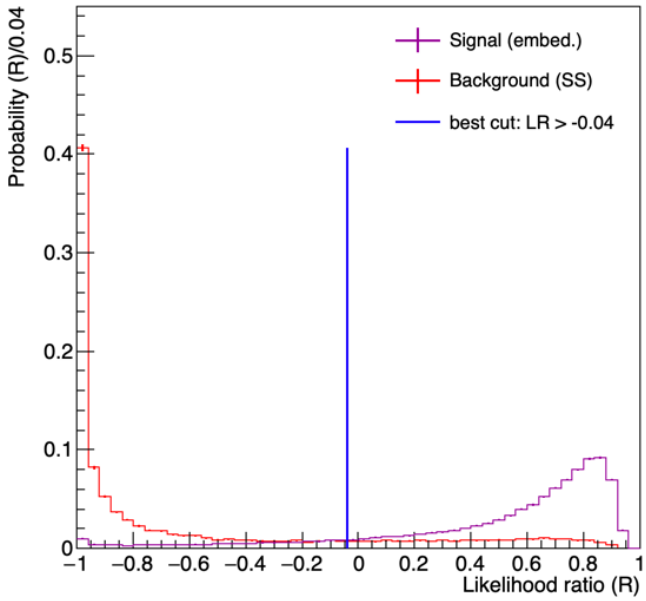

Figure 5.3: The Likelihood ratio R distribution of signal (embed.) and background (SS).

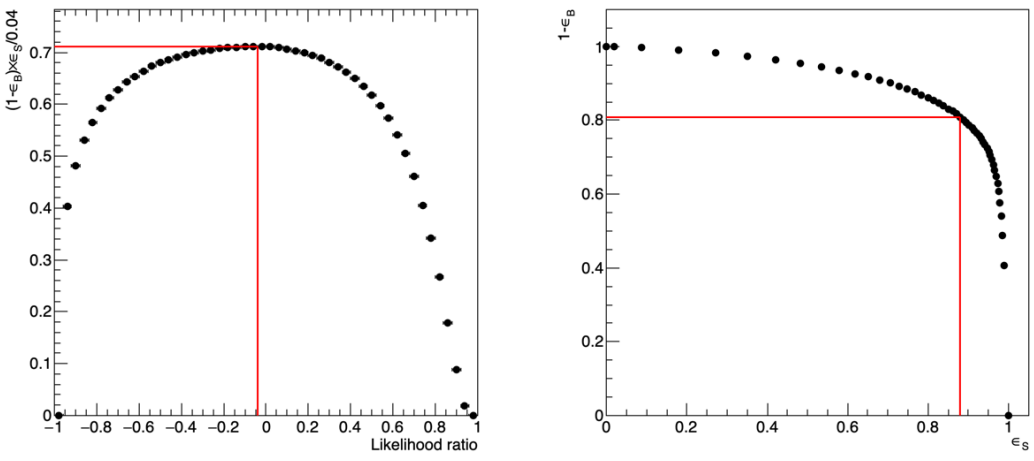

(a) $(1-\epsilon_B) \times \epsilon_S$ vs. Likelihood ratio (R)

(b) $(1-\epsilon_B)$ vs. ϵ_S

Figure 5.4: Performance of the Likelihood ratio (R).

5.2 The Υ signal extraction

The centrality and p_T^{Υ} bins we chose are 0-10%, 10-30%, 30-60% and 0-2 GeV/c, 2-4 GeV/c, 4-10 GeV/c, where the centrality is determined by the Global tracks with Heavy Flavor Tracker [5]. As described in Section 4.3.2, the shapes of the Υ signal is fixed by the embedding samples. The fitting parameter, $rate$ indicates the relative contribution from the first Gaussian, M indicates the mean of the double Gaussian ,and σ_1 and σ_2 indicate the widths of the two Gaussians. Fig. 5.5 $-$ 5.7 show the shapes of Υ(1S), Υ(2S) and Υ(3S) fitted by double Gaussians functions as shown in the red solid lines, and these fits are used for the systematic uncertainty estimation of the signal extraction. The p_T weighted TPC track pairs are used as background functions which are shown in Fig. 5.8. The polynomial function is used to describe the p_T weighted TPC track pairs and considered in the systematic uncertainty of the signal extraction.

The spectra of the opposite-sign dimuon invariant mass and the corresponding fit in each Υ p_T and centrality bin are shown in Fig 5.9. The red solid lines are the total fits, the red dashed lines are the background, and the blue, pink, and green area show the Υ(1S), Υ(2S), and the Υ(3S) signal, respectively. The numbers of Υ(3S) reach the lower limit in the fit (zero event) in several centrality and p_T bins (10-30%, 30-60%, 0-2 GeV/c, 2-4 GeV/c). The upper limits of the corrected number of Υ(3S) in these bins will be described in Section 5.4.

5.3 Efficiencies correction

The efficiencies of muon and the acceptances of Υs are needed to calculate the corrected yields of Υ. In this analysis, we used the candidate-by-candidate weighting method to correct the number of Υ ($N_{\Upsilon}^{corrected}$) in individual Υ p_T and centrality bins. This method was used in the J/ψ production measurement using Run 13 data in the STAR experiment [20]. $N_{\Upsilon}^{corrected}$ is defined as $N_{\Upsilon}^{corrected} = \sum_{i=1}^{N_{\Upsilon}} w_i$, where the inverse weight (w^{-1}) is defined as the acceptance of the detector multiplied by the efficiencies of each muon candidate which is defined as follow, $w^{-1} = A_{\Upsilon}(p_T^{\Upsilon}, y^{\Upsilon}) \times \epsilon_{TPC}^{\mu_1}(cent., \eta^{\mu}, \phi^{\mu}) \times \epsilon_{TPC}^{\mu_2}(cent., \eta^{\mu}, \phi^{\mu}) \times A_{MTD}(p_T^{\Upsilon}, y^{\Upsilon}) \times \epsilon_{MTD}^{\mu_1}(p_T^{\mu}, bkg^{\mu}, mod^{\mu}) \times \epsilon_{MTD}^{\mu_2}(p_T^{\mu}, bkg^{\mu}, mod^{\mu}) \times \epsilon_{\mu ID}^{\mu_1}(p_T^{\mu}) \times \epsilon_{\mu ID}^{\mu_2}(p_T^{\mu})$,

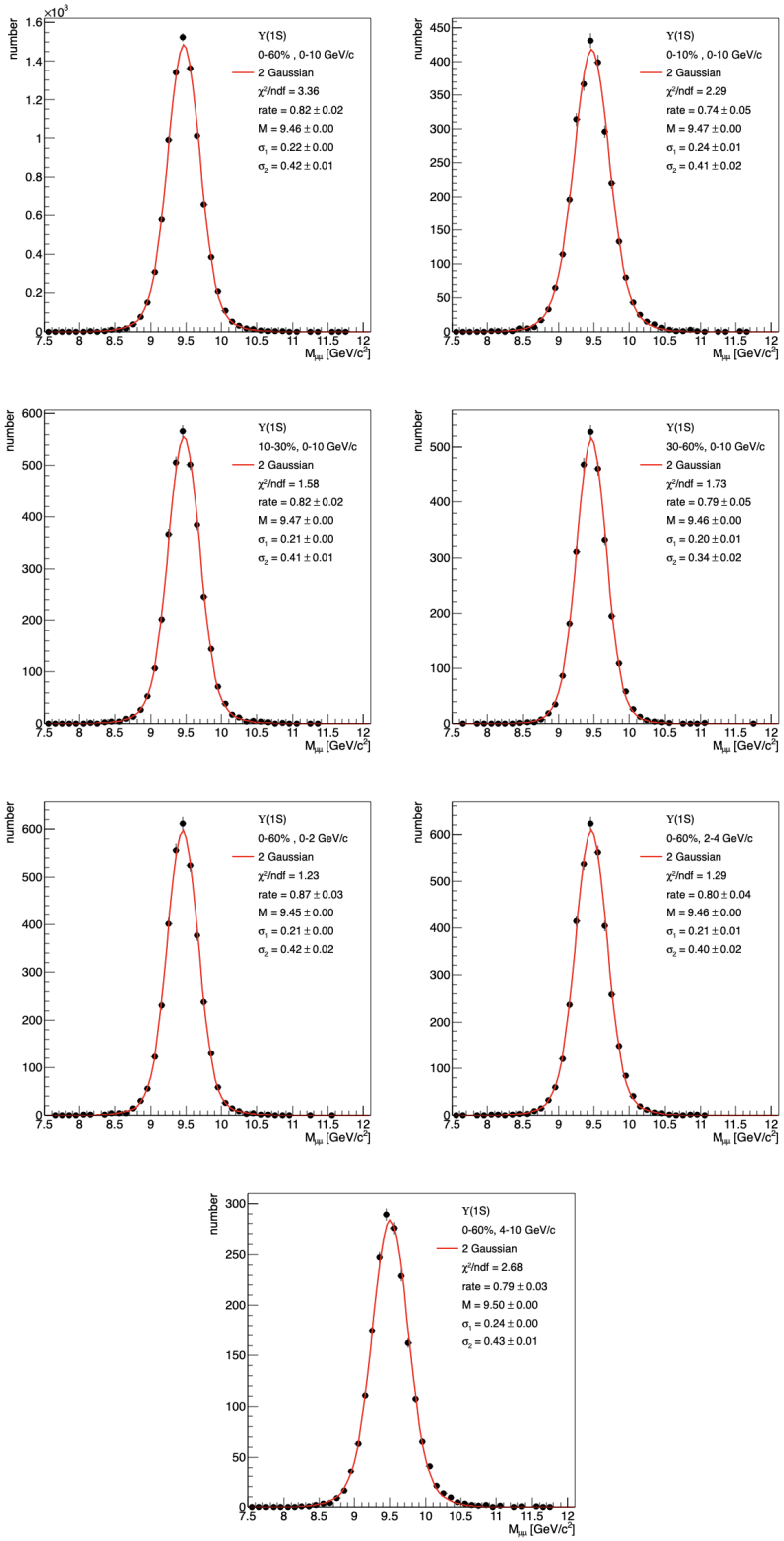

Figure 5.5: The Υ(1S) signal shape and the corresponding fit in each Υ p_T and centrality bin.

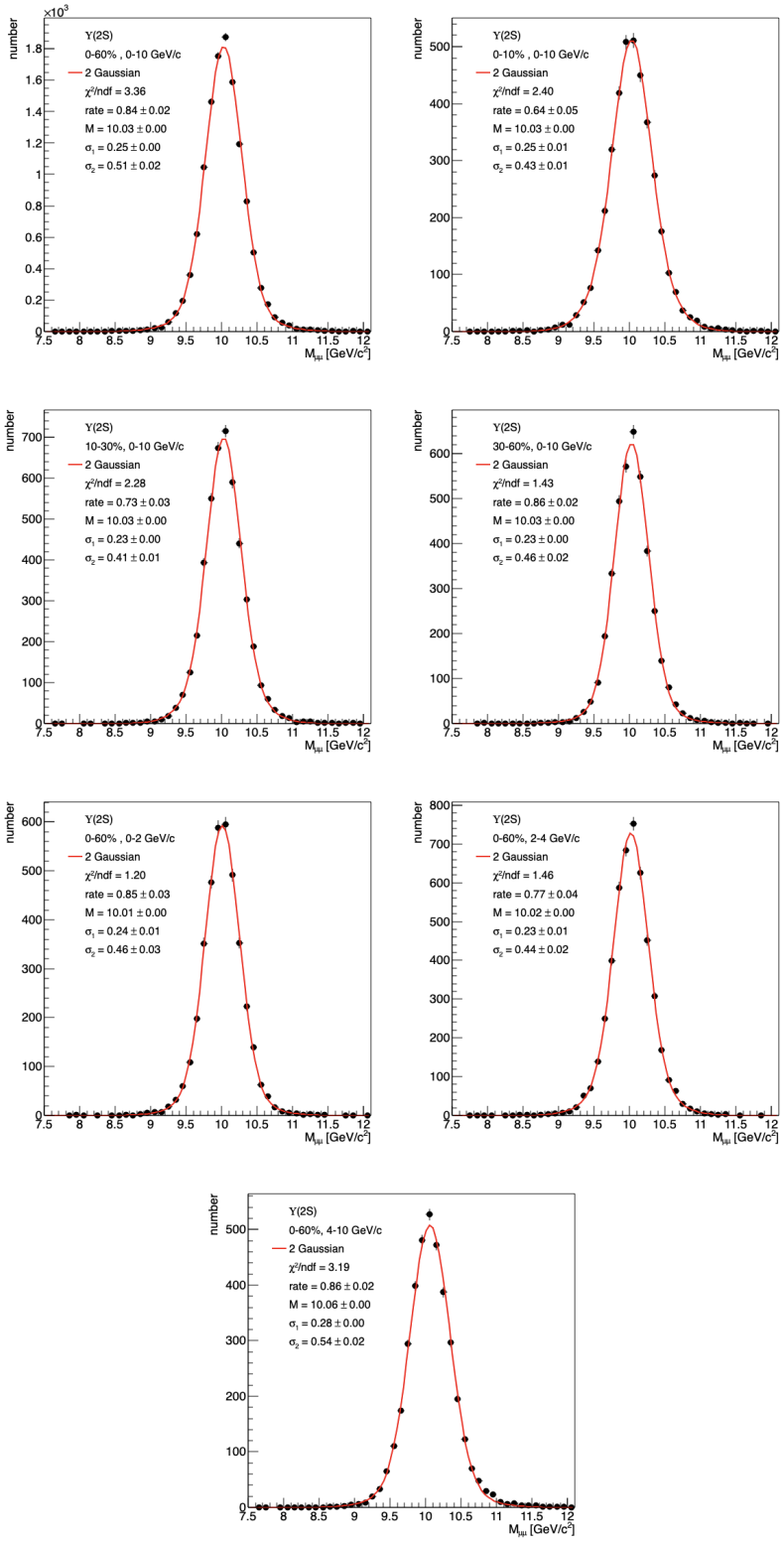

Figure 5.6: The Υ(2S) signal shape and the corresponding fit in each Υ p_T and centrality bin.

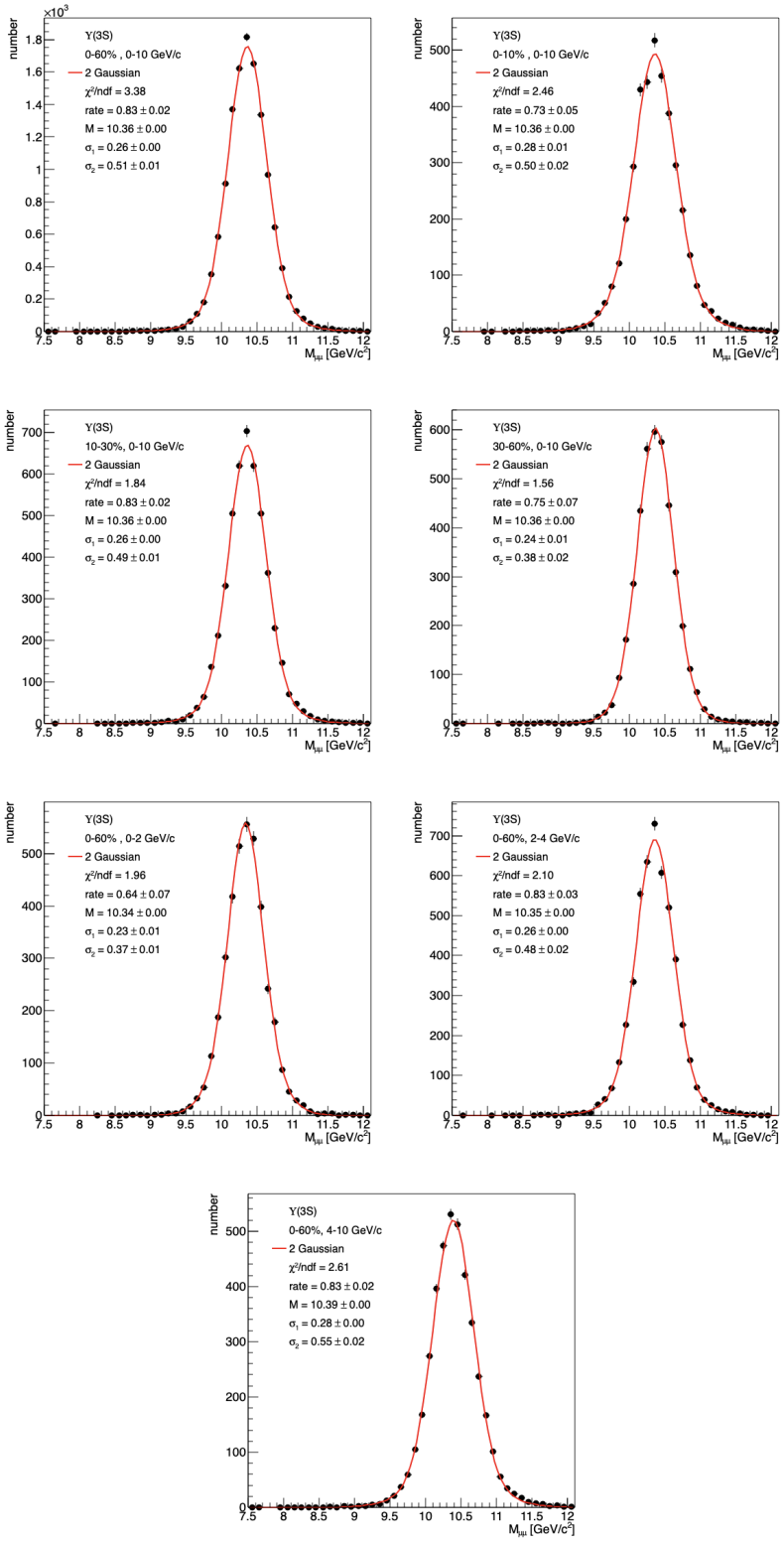

Figure 5.7: The Υ(3S) signal shape and the corresponding fit in each Υ p_T and centrality bin.

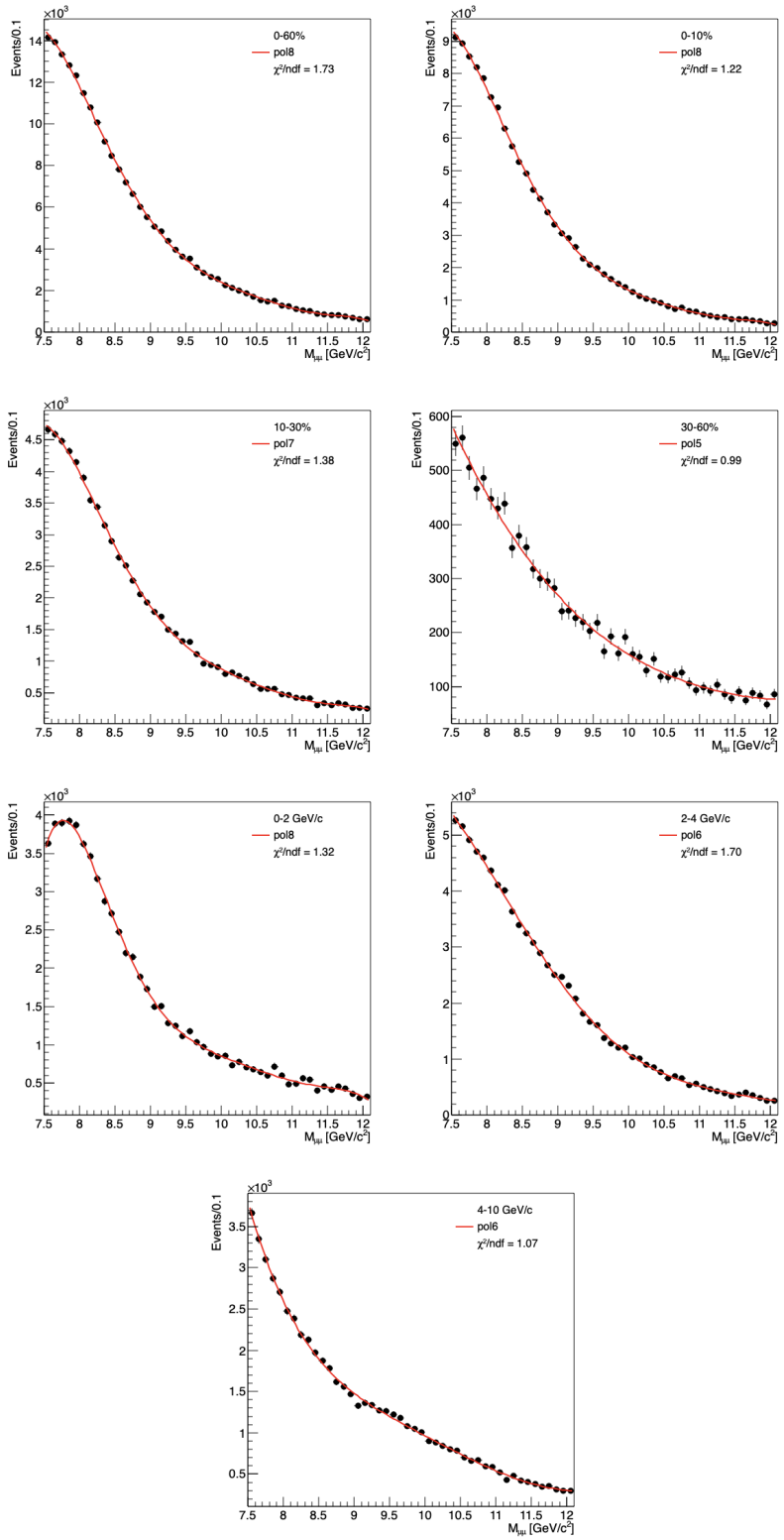

Figure 5.8: The p_T weighted TPC track pairs and the corresponding fit in each Υ p_T and centrality bin.

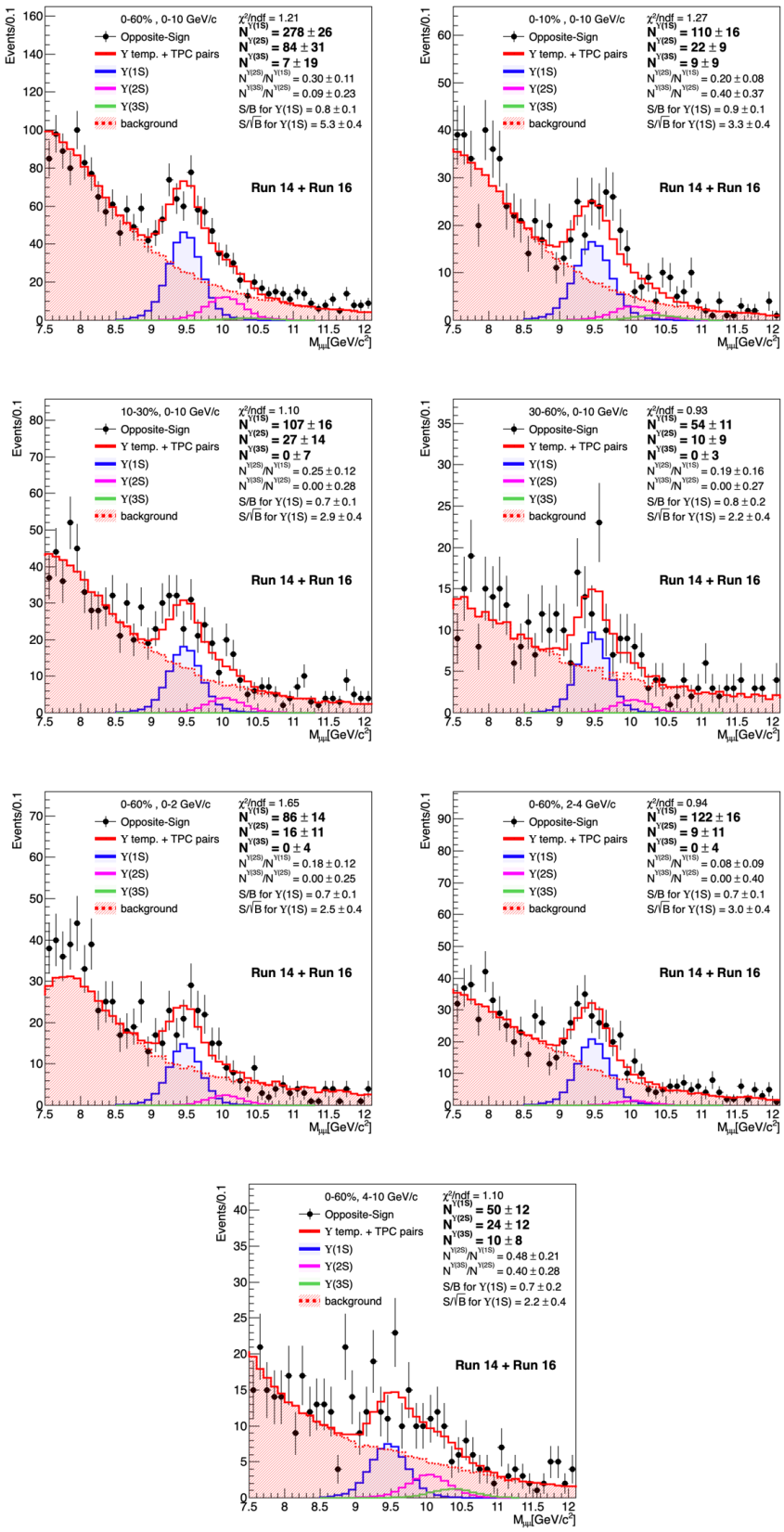

Figure 5.9: Υ signals and the corresponding fits in individual Υ centrality and p_T bins.

where A_Y is the kinematic acceptance of Υ due to the kinematic cuts on muons. ϵ_{TPC} is the TPC tracking efficiency of muon candidates. $cent.$ is the centrality of the event. A_{MTD} is the MTD geometry acceptance for Υ. ϵ_{MTD} is the MTD related efficiencies which include the MTD trigger efficiency as a function of muon p_T ($\epsilon_{MTD\ trigger}(p_T^\mu)$), the MTD response efficiency as a function of p_T, MTD backleg and MTD module ($\epsilon_{MTD\ response}(p_T^\mu, bkg^\mu, mod^\mu)$), and the MTD matching efficiency as a function of p_T ($\epsilon_{MTD\ matching}(p_T^\mu)$). $\epsilon_{\mu ID}$ is the muon identification efficiency of muon candidates. The ϵ^{μ_1} and ϵ^{μ_2} indicate the efficiencies of each daughter muons.

5.3.1 Υ kinematic acceptance

To obtain the kinematic acceptance of Υ, we used a particle gun ToyMC generator, which was used in the Run 13 analysis, to generate the acceptance maps in several polarized cases as a function of Υ p_T and rapidity. The unpolarized Υs are assumed in the R_{AA} measurements. Fig. 5.10 (a), (b), and (c) shows the kinematic acceptance maps with un-polarized assumption for Υ(1S), Υ(2S) and Υ(3S), respectively.

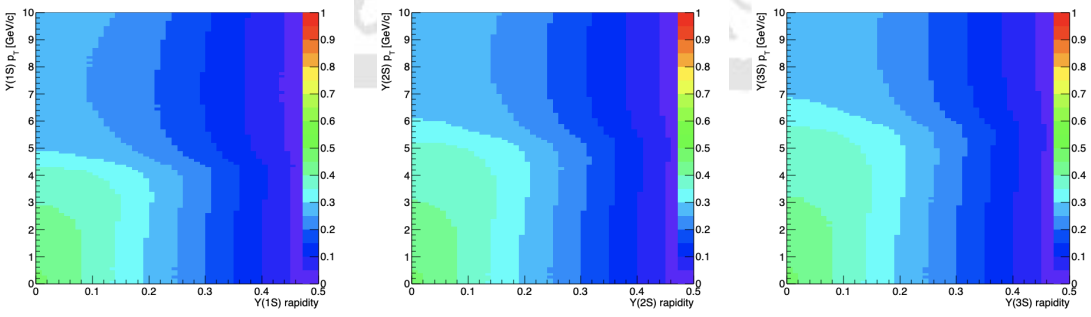

(a) (b) (c)

Figure 5.10: The kinematic acceptance maps of (a) Υ(1S), (b) Υ(2S), (c) Υ(3S) with un-polarized assumption.

5.3.2 TPC tracking efficiency

The TPC tracking efficiency is evaluated from the $\Upsilon \rightarrow \mu^+\mu^-$ embedding samples and it is defined as $\epsilon^{\mu}_{TPC} = \frac{N^{\mu}_{tracked\ by\ TPC}}{N^{\mu}_{truth}}$, where $N_{tracked\ by\ TPC}$ is the number of muons reconstructed by the TPC and required the track quality selections described in section 4.1, N_{truth} is the number of muons generated in MC truth level within the kinematic acceptance described in section 4.3.2.

Since the p_T cuts on muons are 4 and 3 GeV/c which are in the plateau region of the TPC efficiency, the efficiency is only dependent on centrality, ϕ, and η. Due to the difference of TPC performance between data and embedding samples, an additional correction factor is applied in the embedding samples. The correction factors as a function of p_T and ϕ for Run 14 and Run 16 are shown in Fig. 5.11(a) [11] and Fig. 5.11(b) [5], respectively. The TPC tracking efficiencies considered the correction factors as a function of centrality, η and ϕ for Run 14 and Run 16 are shown in Fig. 5.12 and Fig. 5.13, respectively.

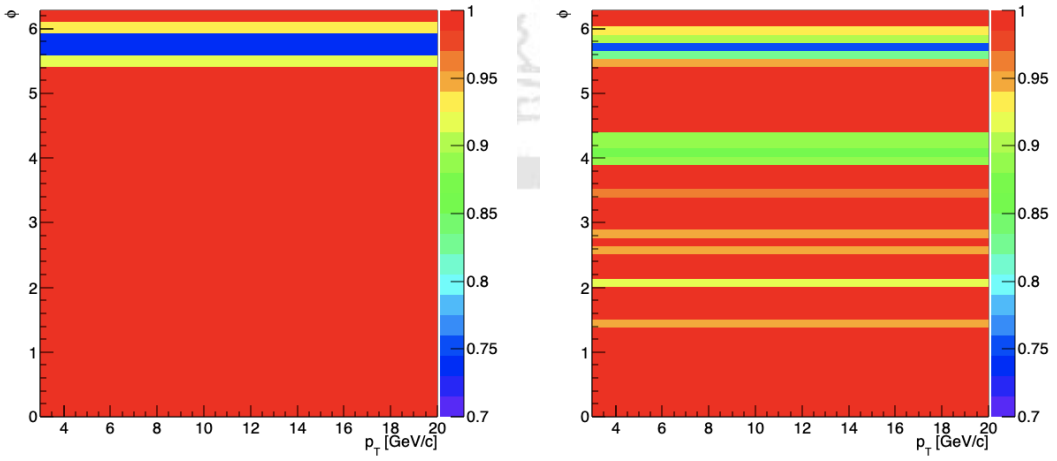

(a) (b)

Figure 5.11: Additional correction factor for TPC tracking efficiency for (a) Run 14 [11] and (b) Run 16 [5].

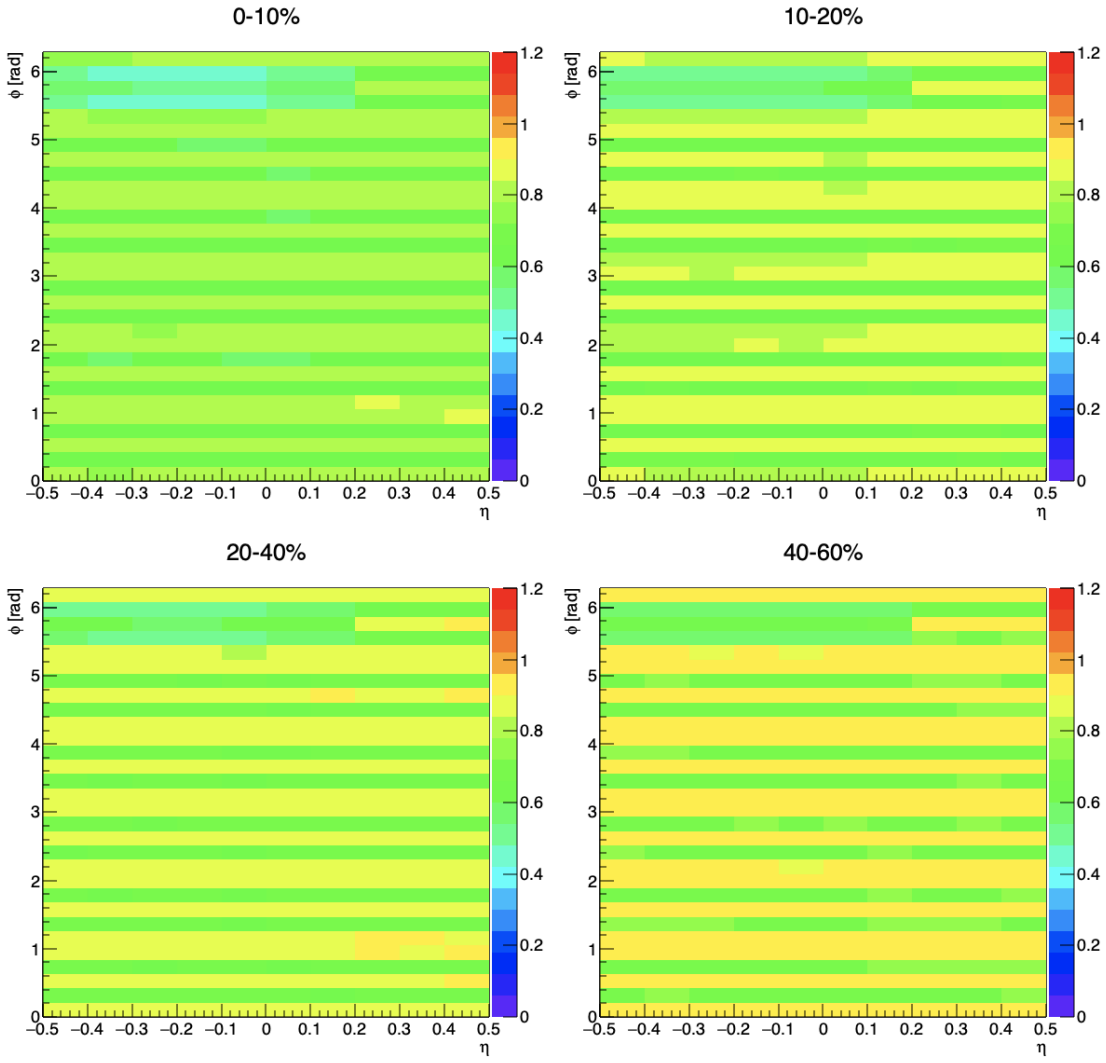

Figure 5.12: TPC tracking efficiencies as a function of centrality, ϕ, and η for Run 14.

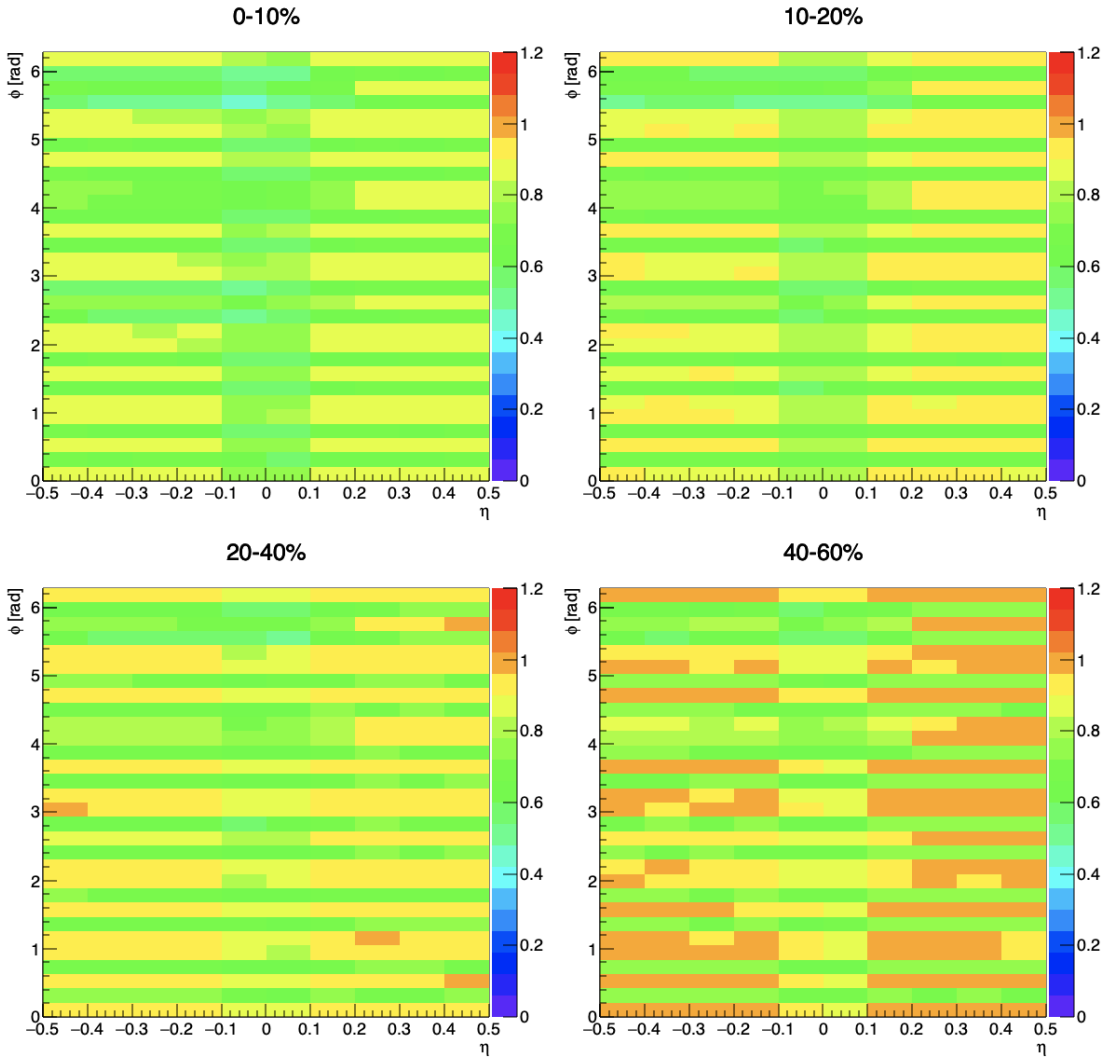

Figure 5.13: TPC tracking efficiencies as a function of centrality, ϕ, and η for Run 16.

5.3.3 Υ MTD geometry acceptance

This acceptance is defined as the probability of the muon can be extrapolated to the MTD module in the region of the MTD radius. To estimate the MTD geometry acceptance of Υ, we first built the MTD geometry acceptance for single muon as a function of muon p_T, η, and ϕ using the $\Upsilon \to \mu^+\mu^-$ embedding sample and they are shown in Fig. 5.14 and Fig. 5.15 for Run 14 and Run 16, respectively. Then this acceptance is applied on the $\Upsilon \to \mu^+\mu^-$ ToyMC sample using binomial distributions to correct the probability of the muon candidates falling into the MTD acceptance. Due to the similarity of the MTD geometry acceptances of Υ using the single muon acceptances from Run 14 and Run 16, the final MTD acceptance map is base on Run 14 embedding.

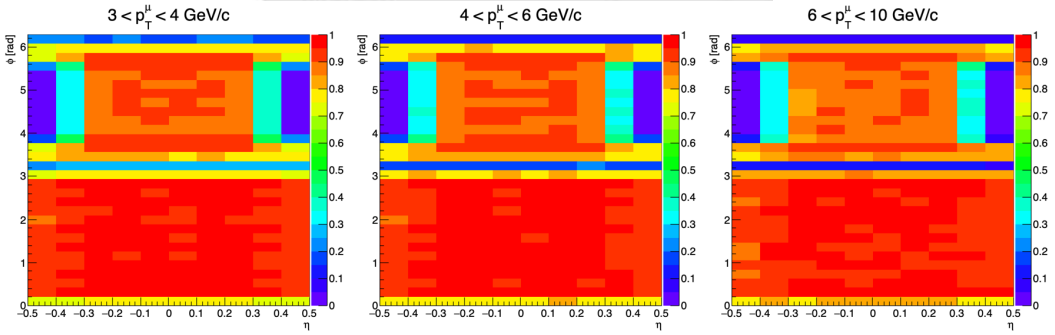

Figure 5.14: The MTD geometry acceptance of single muon for Run 14.

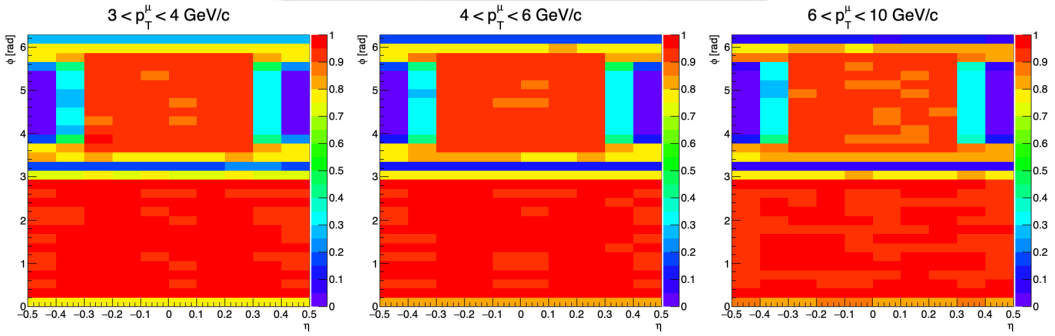

Figure 5.15: The MTD geometry acceptance of single muon for Run 16.

5.3.4 MTD related efficiency

The MTD related efficiencies include three parts: the MTD trigger efficiency, the MTD response efficiency, and the MTD matching efficiency. The MTD trigger efficiency consists

of MTD trigger electronics and online trigger time window cut. The details of the MTD trigger efficiency can be found in the analysis notes for the Run 14 J/ψ R_{AA} study [11]. The MTD response efficiency is evaluated from the cosmic ray data by extrapolating the tracks to the MTD radius and counting the fraction of tracks that generate corresponding MTD hits when falling into the MTD active area. The response efficiency is also evaluated similarly in the embedding samples. The differences between the cosmic ray data and the embedding are applied to the embedding samples. The efficiency is estimated module-by-module, so it is the efficiency as a function of the muon p_T, the responded MTD backleg, and module. The MTD trigger efficiency and the MTD response efficiency for Run 14 and Run 16 can be found in [11] and [5], respectively.

The MTD matching efficiency is evaluated from the embedding samples and is defined as $\epsilon^{\mu}_{MTD\ matching} = \frac{N^{\mu}_{matched}}{N^{\mu}_{projected}}$, where $N^{\mu}_{matched}$ is the number of muon tracks that can be matched to the MTD hits, and $N^{\mu}_{projected}$ is the number of muon tracks that can be projected to the MTD module. The MTD matching efficiency as a function of muon p_T for Run 14 (black points) and Run 16 (blue points) are shown in Fig. 5.16.

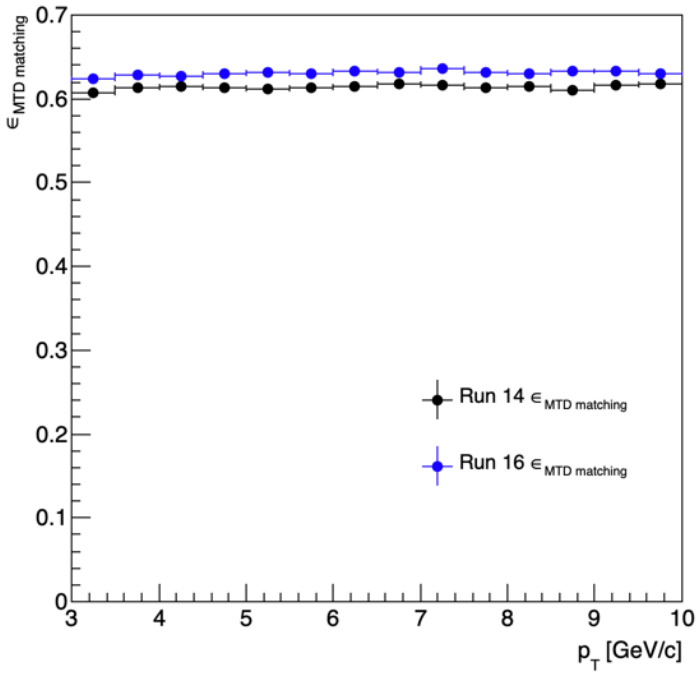

Figure 5.16: MTD matching efficiency as a function of muon p_T for Run 14 (black points) and Run 16 (blue points).

5.3.5 Muon identification efficiency

The muon identification efficiency is defined as the probability of the muons pass the Likelihood Ratio selection described in Section 5.1. and as defined as $\epsilon^{\mu}_{\mu ID} = \frac{N^{\mu}_{\mu ID}}{N^{\mu}_{matched}}$, where $N^{\mu}_{\mu ID}$ is the number of muons pass the Likelihood Ratio selection. Similar to TPC tracking efficiency and MTD matching efficiency, the muon identification efficiency is evaluated from embedding samples, too. The muon identification efficiency as a function of muon p_T for Run 14 (black points) and Run 16 (blue points) are shown in Fig. 5.17.

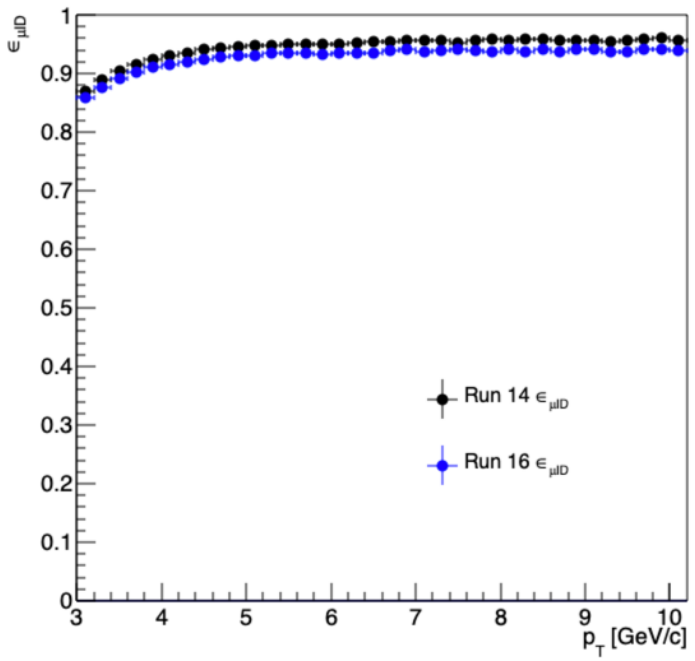

Figure 5.17: The muon identification efficiency as a function of muon p_T for Run 14 (black points) and Run 16 (blue points).

5.3.6 The efficiency-corrected yields of Υ

The candidate-by-candidate weighting method as described in Section 5.3 is used to correct the number of Υ in individual Υ centrality and p_T bins. The actual values of the efficiency-corrected numbers of Υ(1S), Υ(2S) and Υ(3S) are summarized in Table 5.1.

	centrality & p_T bins	Signal numbers
	centrality: 0-10%	5774 $\pm$ 826
	centrality: 10-30%	4391 $\pm$ 663
	centrality: 30-60%	2820 $\pm$ 568
Υ(1S)	0 < p_T < 2 GeV/c	4767 $\pm$ 778
	2 < p_T < 4 GeV/c	5078 $\pm$ 683
	4 < p_T < 10 GeV/c	3054 $\pm$ 752
	centrality: 0-10%	1109 $\pm$ 469
	centrality: 10-30%	1071 $\pm$ 558
	centrality: 30-60%	501 $\pm$ 441
Υ(2S)	0 < p_T < 2 GeV/c	867 $\pm$ 610
	2 < p_T < 4 GeV/c	380 $\pm$ 443
	4 < p_T < 10 GeV/c	1278 $\pm$ 639
	centrality: 0-10%	436 $\pm$ 439
	centrality: 10-30%	upper limit case
	centrality: 30-60%	0 $\pm$ 135
Υ(3S)	0 < p_T < 2 GeV/c	upper limit case
	2 < p_T < 4 GeV/c	upper limit case
	4 < p_T < 10 GeV/c	487 $\pm$ 416

Table 5.1: The efficiency-corrected numbers of Υ(1S), Υ(2S) and Υ(3S) in individual Υ centrality and p_T bins.

5.4 The upper limit of the number of Υ(3S)

The raw numbers of Υ(3S) reach the lower limit in the fit (zero event) in several p_T and centrality bin, such as 10-30%, 30-60%, 0-2 GeV/c, 2-4 GeV/c as described in section 5.2. To estimate the upper limit of the numbers of Υ(3S) in these centrality and p_T bins, we randomly generated 10,000 opposite-sign dimuon mass distributions based on the data and the corresponding statistical uncertainties, and extracted the number of Υ(3S). The 95% confident level (C.L.) limit is set to be the point where the intergrated area of the numbers of Υ(3S) distribution is 95% of the total area. The numbers of Υ(3S) distributions in 10-30%, 30-60%, 0-2 GeV/c, 2-4 GeV/c are shown in Fig. 5.18. The detailed values of the upper limits are summarized in Table 5.2.

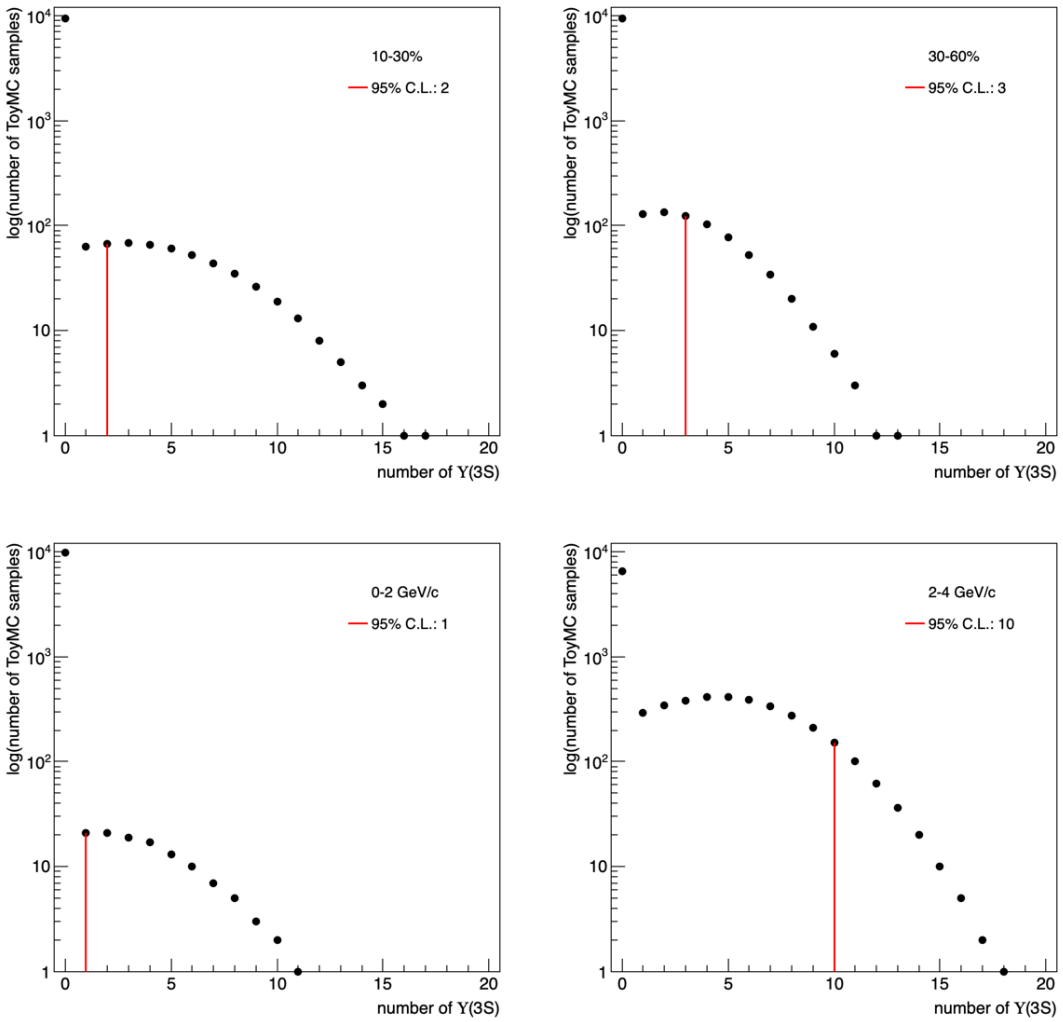

Figure 5.18: The numbers of Υ(3S) distributions in 10-30%, 30-60%, 0-2 GeV/c, and 2-4 GeV/c.

centrality & p_T bins	95% C.L. upper limit
10-30%	2
30-60%	3
0-2 GeV/c	1
2-4 GeV/c	10

Table 5.2: The 95% upper limits of the raw Υ(3S) in 10-30%, 30-60%, 0-2 GeV/c, and 2-4 GeV/c.

The total Υ efficiency is evaluated from the raw number and the corrected number of Υ. Due to the low statistics, the total Υ(3S) efficiency is assumed to be similar to the total Υ(1S) efficiency. The upper limit of the corrected number of Υ(3S) is estimated by the 95% C.L. limit described above corrected by the total Υ(1S) efficiency. The total Υ(1S) efficiency and total Υ(2S) efficiency in each centrality and p_T bin and the detailed values of the upper limits of efficiency-corrected Υ(3S) are summarized in Table 5.3 and Table 5.4, respectively.

	centrality & p_T bins	Total efficiency
Υ(1S)	0-10%	1.91% $\pm$ 2.46%
	10-30%	2.44% $\pm$ 2.83%
	30-60%	1.91% $\pm$ 3.95%
	0-2 GeV/c	1.80% $\pm$ 2.90%
	2-4 GeV/c	2.40% $\pm$ 2.43%
	4-10 GeV/c	1.64% $\pm$ 5.17%
Υ(2S)	0-10%	1.98% $\pm$ 11.30%
	10-30%	2.52% $\pm$ 14.73%
	30-60%	2.00% $\pm$ 23.42%
	0-2 GeV/c	1.85% $\pm$ 19.71%
	2-4 GeV/c	2.37% $\pm$ 27.28%
	4-10 GeV/c	1.88% $\pm$ 13.87%

Table 5.3: The total Υ(1S) efficiency and total Υ(2S) efficiency in each centrality and p_T bin.

centrality & p_T bins	95% C.L. upper limit
10-30%	82
30-60%	157
0-2 GeV/c	56
2-4 GeV/c	417

Table 5.4: The 95% upper limits of the efficiency-corrected ϒ(3S) in 10-30%, 30-60%, 0-2 GeV/c, and 2-4 GeV/c.

5.5 Systematic uncertainties

Several sources of the systematic uncertainty for the measurement of ϒ R_{AA} are considered: (1) the extraction of the numbers of the ϒ signals; (2) the efficiencies used to correct the numbers of the ϒ signals.

5.5.1 Signal extraction

The different combinations of the signal and background functions are used to extract the numbers of ϒ signals and to estimate the systematic uncertainty. The systematic uncertainty from the signal extraction is estimated by the maximum deviation from the average of all the combinatory (new central) for each p_T and centrality bin. The signal functions are: (1) the ϒ signal shapes from embedding; (2) the fits of the ϒ signal shapes as described in section 5.2; (3) the fits of the ϒ signal shapes, but changes the widths of the double Gaussians by adding twice the errors to the original widths; (4) the fits of the ϒ signal shapes, but changes the widths of double Gaussians by subtracting twice the errors to the original widths. The background functions are (1) the p_T weighted TPC track pairs and (2) the corresponding polynomial fits as described in section 5.2.

The numbers of ϒ extracted from different fitting functions in each p_T and centrality bin for ϒ(1S), ϒ(2S) and ϒ(3S) are shown in Fig. 5.19, Fig. 5.20 and Fig. 5.21, respectively. The results from each fitting function are shown in different colors with open squares, the new central values are shown in black solid circles and the slashed area indicates the systematic

uncertainty from the signal extraction. To evaluate the systematic uncertainties for Υ(3S) in the upper limit cases (10-30%, 30-60%, 0-2 GeV/c, 2-4 GeV/c), we used the same method as described in Section 5.4 to estimate the upper limits of these centrality and p_T bins but with the different fitting functions which we described above. Then the uncertainties for Υ(3S) in the upper limit cases are evaluated by the maximum deviation from the average method as described above. The systematic uncertainties for Υ(1S), Υ(2S) and Υ(3S) are shown in Fig. 5.22. The actual numbers of Υ(1S), Υ(2S) and Υ(3S) are summarized in Table 5.5.

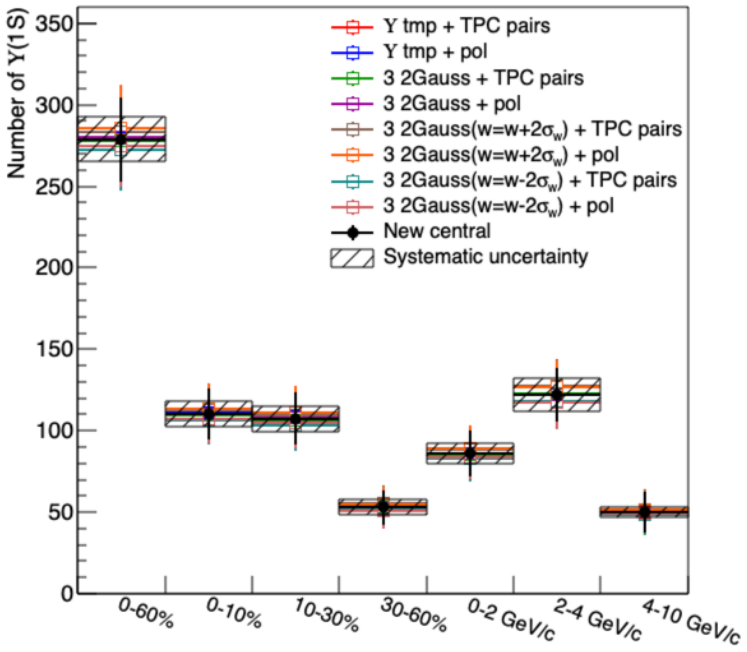

Figure 5.19: Number of Υ(1S) extracted from different fitting functions in each p_T and centrality bin.

5.5.2 TPC tracking efficiency

To evaluated the systematic uncertainty from the TPC tracking efficiency, we varied the selections of the track quality applied to the muon candidates, and then compared the background (the TPC track pairs) subtracted invariant mass distribution. The selections of the track quality include the DCA, NHitsfit, and NHitsDedx calculation and the variations of the cuts are summarized in Table 5.6. Since the different track quality selections don't change the shapes of the muon candidates p_T and the TPC tracks p_T, the p_T weighted TPC

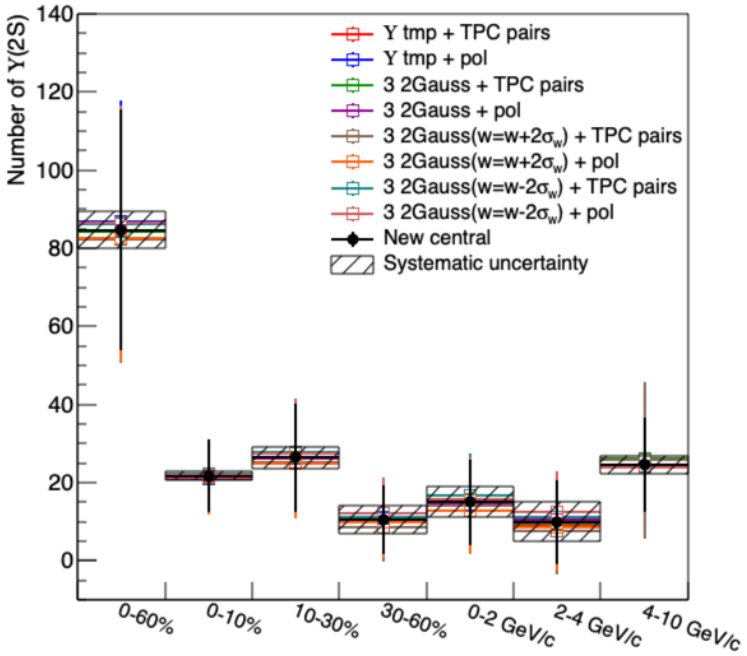

Figure 5.20: Number of Υ(2S) extracted from different fitting functions in each p_T and centrality bin.

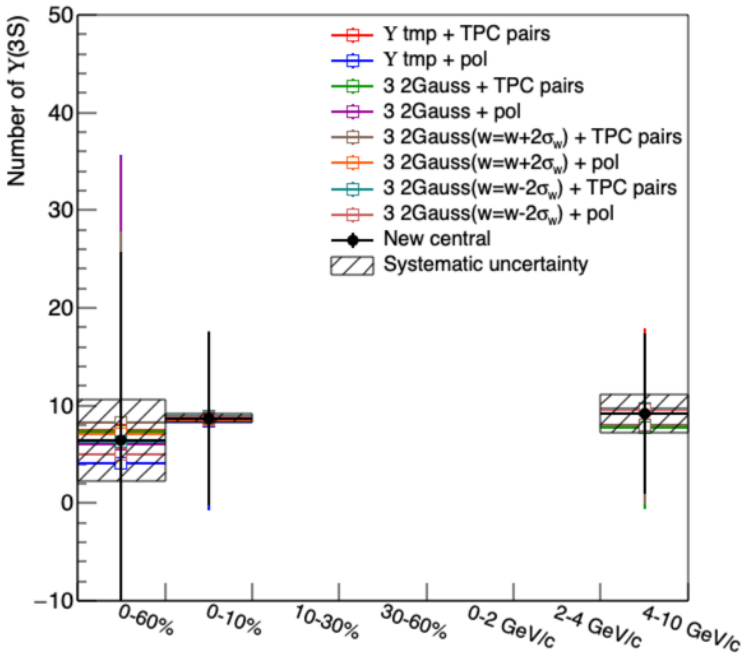

Figure 5.21: Number of Υ(3S) extracted from different fitting functions in each p_T and centrality bin.

	centrality & p_T bins	Signal numbers
	centrality: 0-60%	278 ± 26 ± 14 (4.90%)
	centrality: 0-10%	110 ± 16 ± 8 (6.89%)
	centrality: 10-30%	107 ± 16 ± 8 (7.26%)
Υ(1S)	centrality: 30-60%	54 ± 11 ± 5 (8.89%)
	$0 < p_T < 2$ GeV/c	86 ± 14 ± 6 (7.32%)
	$2 < p_T < 4$ GeV/c	122 ± 16 ± 10 (8.30%)
	$4 < p_T < 10$ GeV/c	50 ± 12 ± 3 (6.74%)
	centrality: 0-60%	84 ± 31 ± 5 (5.51%)
	centrality: 0-10%	22 ± 9 ± 1 (5.27%)
	centrality: 10-30%	27 ± 14 ± 3 (10.81%)
Υ(2S)	centrality: 30-60%	10 ± 9 ± 3 (34.79%)
	$0 < p_T < 2$ GeV/c	16 ± 11 ± 4 (26.01%)
	$2 < p_T < 4$ GeV/c	9 ± 11 ± 5 (50.35%)
	$4 < p_T < 10$ GeV/c	24 ± 12 ± 2 (9.54%)
	centrality: 0-60%	7 ± 19 ± 5 (64.87%)
	centrality: 0-10%	9 ± 9 ± 0 (5.27%)
	centrality: 10-30%	upper limit case (4.37%)
Υ(3S)	centrality: 30-60%	upper limit case (12.82%)
	$0 < p_T < 2$ GeV/c	upper limit case (2.91%)
	$2 < p_T < 4$ GeV/c	upper limit case (0.31%)
	$4 < p_T < 10$ GeV/c	10 ± 8 ± 2 (21.16%)

Table 5.5: The number of Υ(1S), Υ(2S) and Υ(3S) at individual centrality and p_T bin. The first error is statistical and the second one is the systematic uncertainty from signal extraction.

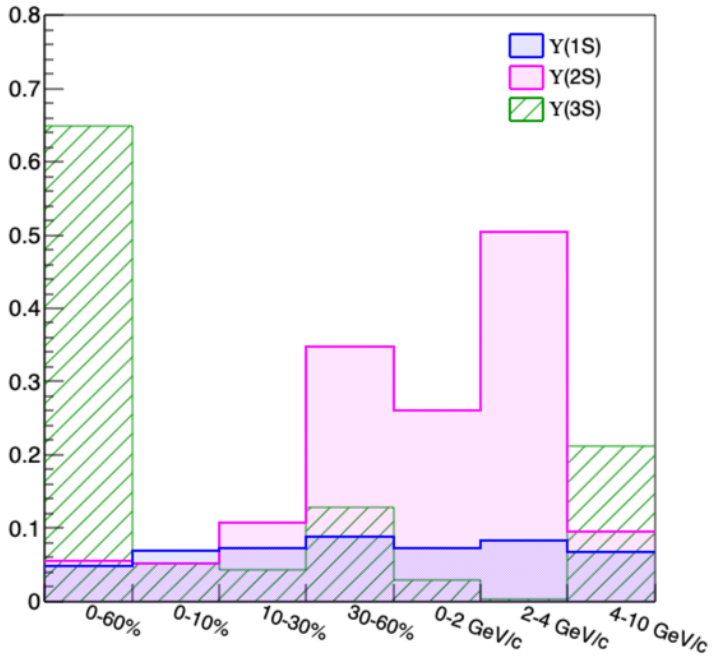

Figure 5.22: Systematic uncertainties from signal extraction for ϒ(1S), ϒ(2S) and ϒ(3S).

track pairs with default cut are used as the background template for all the cases. The ratios of background-subtracted efficiency-corrected opposite-sign mass distribution using different track quality cuts to the default one in individual p_T and centrality bin are shown in Fig. 5.23. The 0^{th} order polynomial function is used to evaluate the uncertainties for ϒ(1S), ϒ(2S) and ϒ(3S). The systematic uncertainties for ϒ(1S), ϒ(2S) and ϒ(3S) in each centrality and p_T bin are shown in Fig. 5.24and the detailed values are summarized in Table 5.7.

The systematic uncertainties for ϒ(3S) in the upper limit cases (10-30%, 30-60%, 0-2 GeV/c, 2-4 GeV/c) are evaluated by the same method as described in Section 5.4. The efficiency-corrected opposite-sign dimuon invariant mass spectrums with different track quality cuts are used to generate the ToyMC samples. The uncertainties for ϒ(3S) in the upper limit cases are evaluated by the maximum deviation from the average method as described in Section 5.6.1. The systematic uncertainties in these cases are shown in Fig. 5.25 and the detailed values are summarized in Table 5.8.

Variables	Default	Variations
DCA	< 1.5	< 1.25 cm, < 1.75 cm
NHitsFit	$\geq$ 15	$\geq$ 25
NHitsDedx	$\geq$ 10	$\geq$ 15

Table 5.6: A summary of the variations of the track quality cuts

centrality & p_T bins	Systematic uncertainty
centrality: 0-60%	7.46%
centrality: 0-10%	12.75%
centrality: 10-30%	5.67%
centrality: 30-60%	12.63%
$0 < p_T < 2$ GeV/c	3.58%
$2 < p_T < 4$ GeV/c	15.14%
$4 < p_T < 10$ GeV/c	4.31%

Table 5.7: The values of the systematic uncertainty from the TPC tracking efficiency for Υ(1S), Υ(2S) and Υ(3S).

centrality & p_T bins	Systematic uncertainty
centrality: 10-30%	114.52%
centrality: 30-60%	89.04%
$0 < p_T < 2$ GeV/c	5.75%
$2 < p_T < 4$ GeV/c	42.06%

Table 5.8: The values of the systematic uncertainty from the TPC tracking efficiency for Υ(3S) in upper limit cases

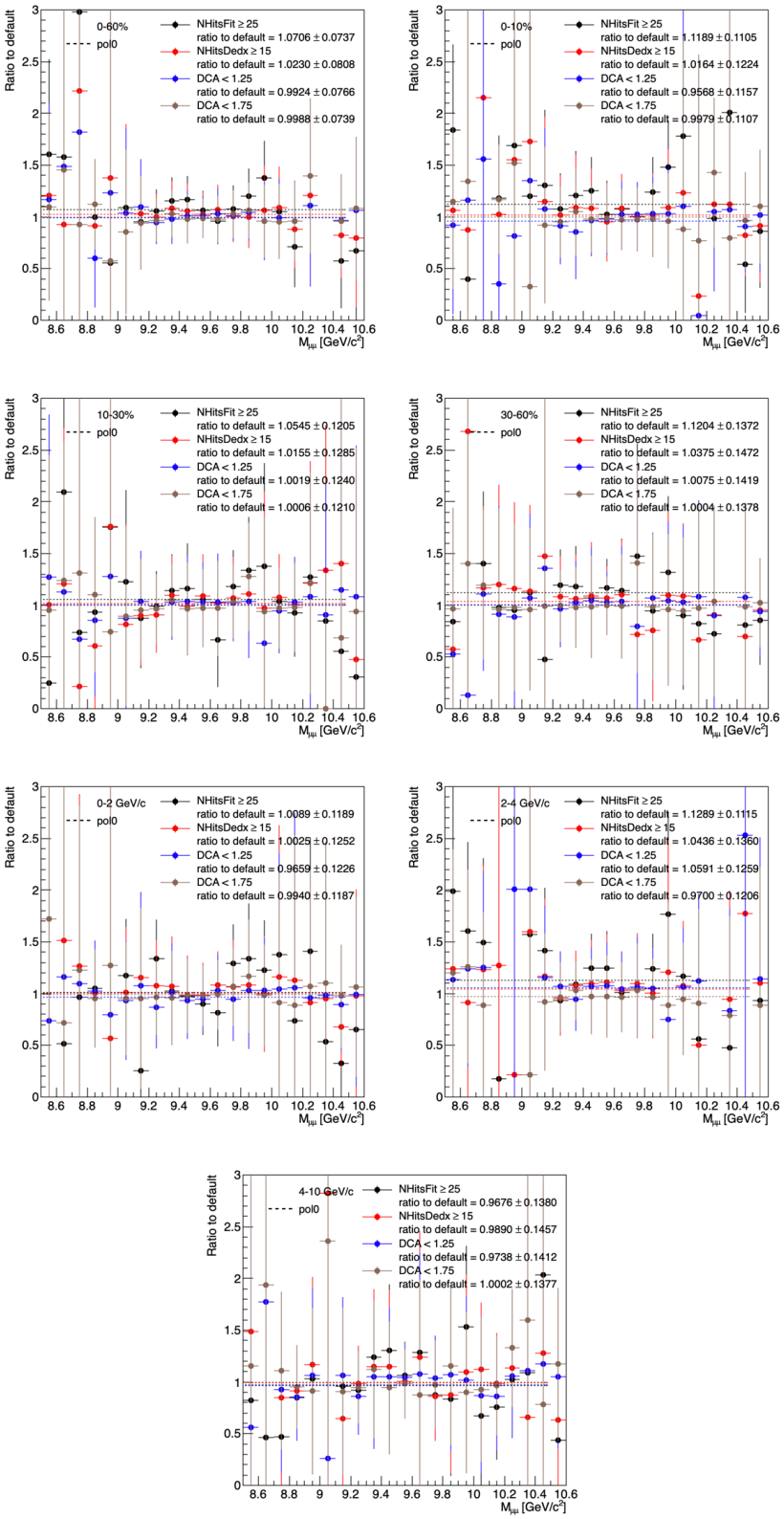

Figure 5.23: Ratios of the TPC tracking efficiency corrected opposite-sign mass subtracted the p_T weighted TPC track pairs using different track quality cuts to the default cuts.

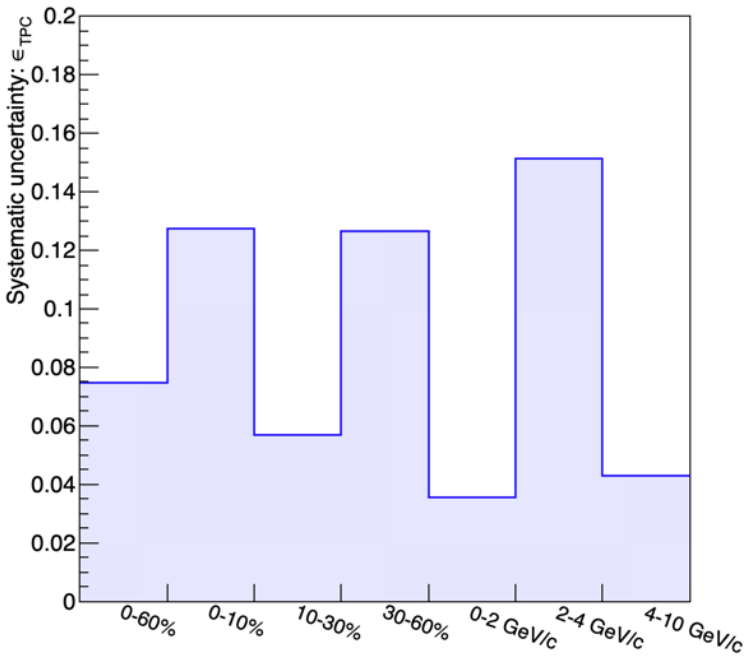

Figure 5.24: Systematic uncertainty from the TPC tracking efficiency for Υ(1S), Υ(2S) and Υ(3S).

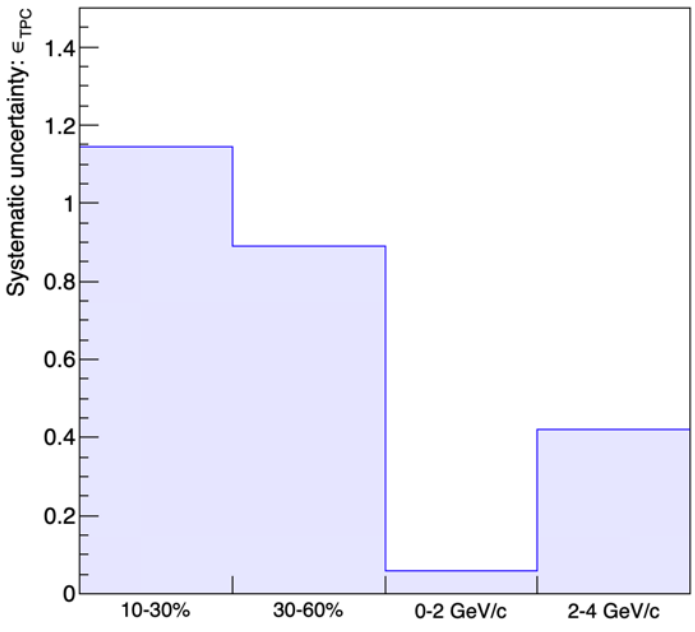

Figure 5.25: Systematic uncertainties from the TPC tracking efficiency for Υ(3S) in upper limit cases

5.5.3 MTD related efficiency

The systematic uncertainties from MTD related efficiencies included the MTD trigger efficiency and the MTD response efficiency are estimated in the Run 14 J/ψ R_{AA} study [11].

The main contribution of the systematic uncertainty from the MTD trigger efficiency is from the procedure to estimate the efficiency associated with the online trigger time window cut. The systematic uncertainty from the MTD trigger electronic efficiency is negligible. There are two sources are used to evaluate the systematic uncertainty from MTD online trigger window cut efficiency: (1) the difference of the mean of ΔTacSum distributions between p+p collisions and Au+Au collisions data; (2) the resolution of p+p collisions and Au+Au collisions data using 1σ limits of the fit functions.

For the systematic uncertainty from the MTD response efficiency, the statistical errors of the cosmic ray data and the difference between backlegs efficiency and the efficiency template in individual MTD modules are used to estimate the systematic uncertainty.

The systematic uncertainties from the MTD trigger efficiency and the MTD response efficiency are centrality independent. The uncertainties for Υ(1S), Υ(2S) and Υ(3S) in each Υ p_T bin are shown in Fig. 5.26. and the detail values are summarized in Table 5.9.

The systematic uncertainties for Υ(3S) in the upper limit cases (10-30%, 30-60%, 0-2 GeV/c, 2-4 GeV/c) are evaluated by the same method as described in Section 5.6.2. The main contribution of the systematic uncertainty from MTD related efficiencies is the MTD trigger efficiency. We used the fits to data and the fits to lower and upper limits of the MTD trigger efficiency [11] to correct the raw yield to generated the ToyMC samples. The systematic uncertainties in these cases are shown in Fig. 5.27 and the detailed values are summarized in Table 5.10.

5.5.4 Muon identification efficiency

Similar method used for the TPC tracking efficiency uncertainty is used to evaluate the systematic uncertainty for muon identification efficiency. The signal efficiency of the default

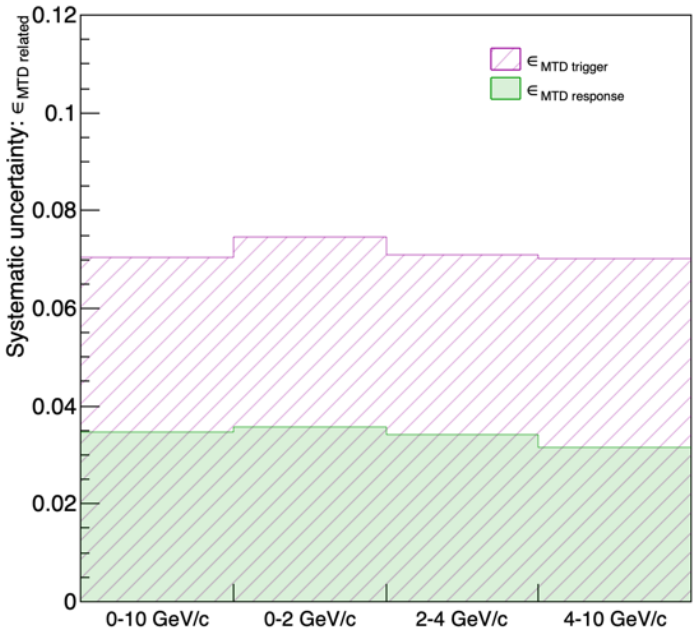

Figure 5.26: Systematic uncertainties from the MTD trigger efficiency and the MTD response efficiency for Υ(1S), Υ(2S) and Υ(3S).

Uncertainty source	p_T bins	Systematic uncertainty
$\epsilon_{MTD\ trigger}$	$0 < p_T < 10$ GeV/c	7.04%
	$0 < p_T < 2$ GeV/c	7.45%
	$2 < p_T < 4$ GeV/c	7.09%
	$4 < p_T < 10$ GeV/c	7.02%
$\epsilon_{MTD\ response}$	$0 < p_T < 10$ GeV/c	3.46%
	$0 < p_T < 2$ GeV/c	3.59%
	$2 < p_T < 4$ GeV/c	3.40%
	$4 < p_T < 10$ GeV/c	3.16%

Table 5.9: The values of the systematic uncertainties from the MTD trigger efficiency and the MTD response efficiency for Υ(1S), Υ(2S) and Υ(3S).

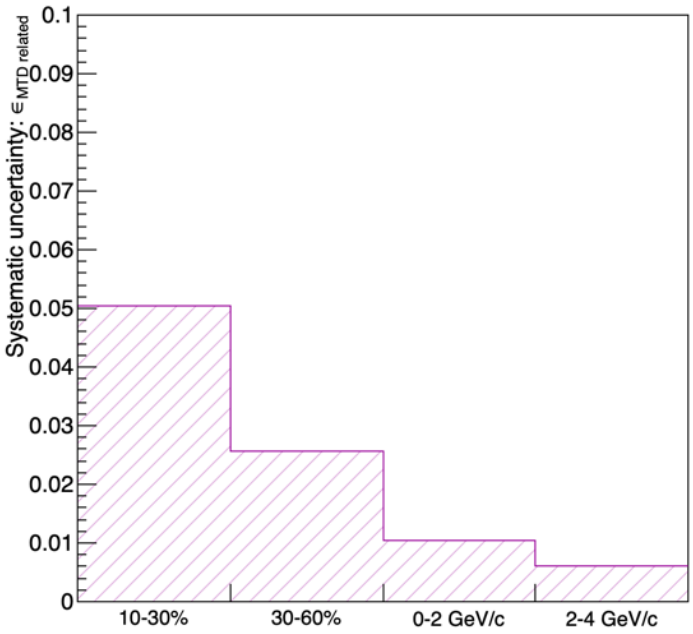

Figure 5.27: Systematic uncertainties from the MTD related efficiencies for Υ(3S) in upper limit cases

centrality & p_T bins	Systematic uncertainty
centrality: 10-30%	5.04%
centrality: 30-60%	2.56%
$0 < p_T < 2$ GeV/c	1.05%
$2 < p_T < 4$ GeV/c	0.62%

Table 5.10: The values of the systematic uncertainty from the MTD related efficiencies for Υ(3S) in upper limit cases

Likelihood Ratio cut (R > -0.04) is about 88%. The cuts are varied to have the corresponding efficiencies of 93% and 83%, R > -0.33 and R > 0.16, respectively, as the source the systematic uncertainty.Since the different Likelihood ratio selection would change the p_T distributions of the muon candidates and the TPC tracks, the p_T weighted TPC track pairs with different Likelihood Ratio selections are used in the corresponding cases. The ratios of efficiency-corrected background-subtracted opposite-sign mass using different Likelihood Ratio cuts to the default one and the corresponding 0^{th} order polynomial fits in individual p_T and centrality bin are shown in Fig. 5.28. The systematic uncertainties for Υ(1S), Υ(2S) and Υ(3S) in each centrality and p_T bin are shown in Fig. 5.29 and the detailed values are summarized in Table 5.11.

The systematic uncertainties for Υ(3S) in the upper limit cases (10-30%, 30-60%, 0-2 GeV/c, 2-4 GeV/c) are evaluated by the same method as described in Section 5.6.2. The systematic uncertainties in these cases are shown in Fig. 5.30 and the detailed values are summarized in Table 5.12.

centrality & p_T bins	Systematic uncertainty
centrality: 0-60%	3.41%
centrality: 0-10%	5.92%
centrality: 10-30%	11.62%
centrality: 30-60%	8.92%
$0 < p_T < 2$ GeV/c	9.16%
$2 < p_T < 4$ GeV/c	11.30%
$4 < p_T < 10$ GeV/c	11.47%

Table 5.11: The values of the systematic uncertainty from muon identification efficiency for Υ(1S), Υ(2S) and Υ(3S).

5.5.5 Total uncertainties

The total uncertainties are evaluated by the quadratic sum of each source described above as $\sigma^2_{total} = \sigma^2_{stat.} + \sum_i \sigma^2_{i,\ sys.}$. The individual uncertainties considered in this analysis

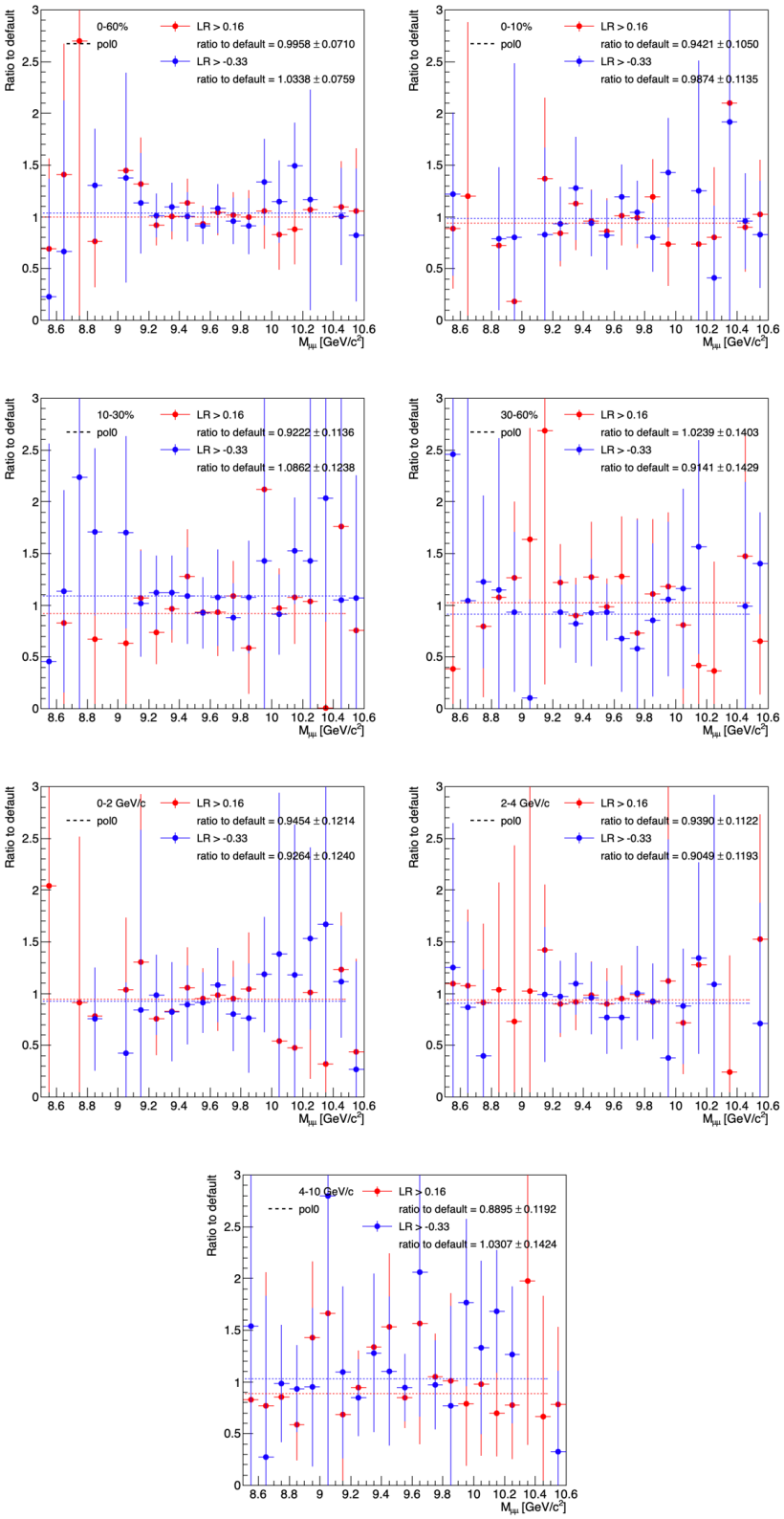

Figure 5.28: Ratios of the muon identification efficiency corrected opposite-sign mass subtracted the p_T weighted TPC track pairs using different Likelihood ratio selections to the default cuts.

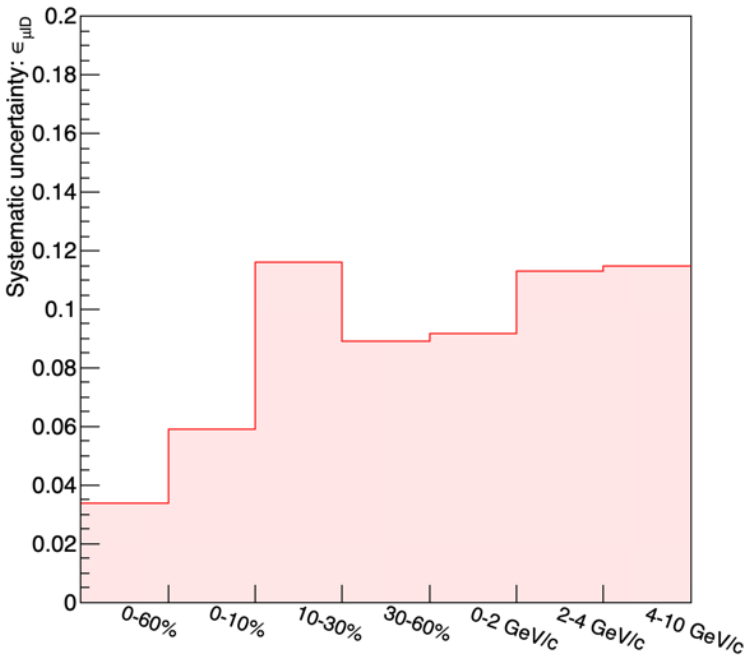

Figure 5.29: Systematic uncertainty from muon identification efficiency for $\Upsilon(1S)$, $\Upsilon(2S)$ and $\Upsilon(3S)$.

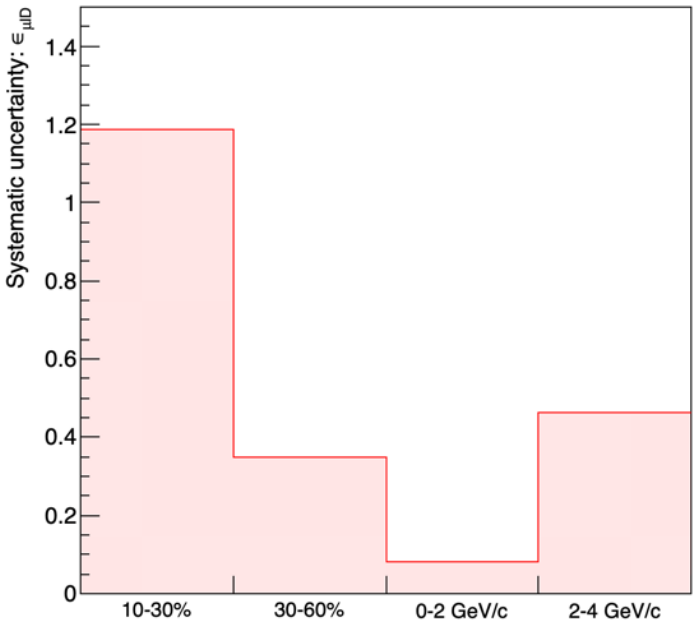

Figure 5.30: Systematic uncertainties from muon identification efficiency for $\Upsilon(3S)$ in upper limit cases

centrality & p_T bins	Systematic uncertainty
centrality: 10-30%	118.61%
centrality: 30-60%	34.74%
$0 < p_T < 2$ GeV/c	8.02%
$2 < p_T < 4$ GeV/c	46.41%

Table 5.12: The values of the systematic uncertainty from muon identification efficiency for ϒ(3S) in upper limit cases

for ϒ(1S), ϒ(2S) and ϒ(3S) are shown in Fig. 5.31, Fig. 5.32 and Fig. 5.33, respectively. The detail values of systematic uncertainties, statistical uncertainties, and the total uncertainties are summarized in Table 5.13. The statistical errors of ϒ(3S) in 10-30%, 30-60%, 0-2 GeV/c, 2-4 GeV/c bins have been considered in the method to estimate upper limit.

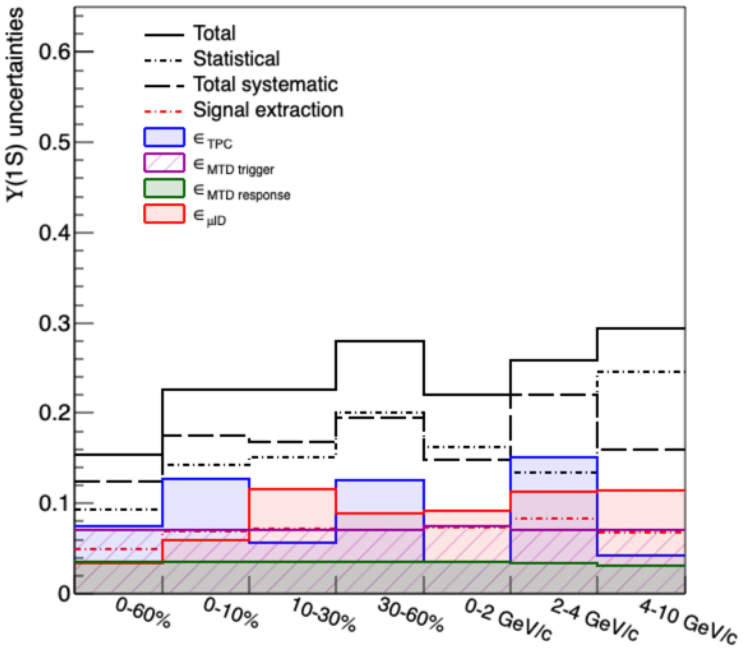

Figure 5.31: The uncertainties from different sources and the total uncertainty for ϒ(1S).

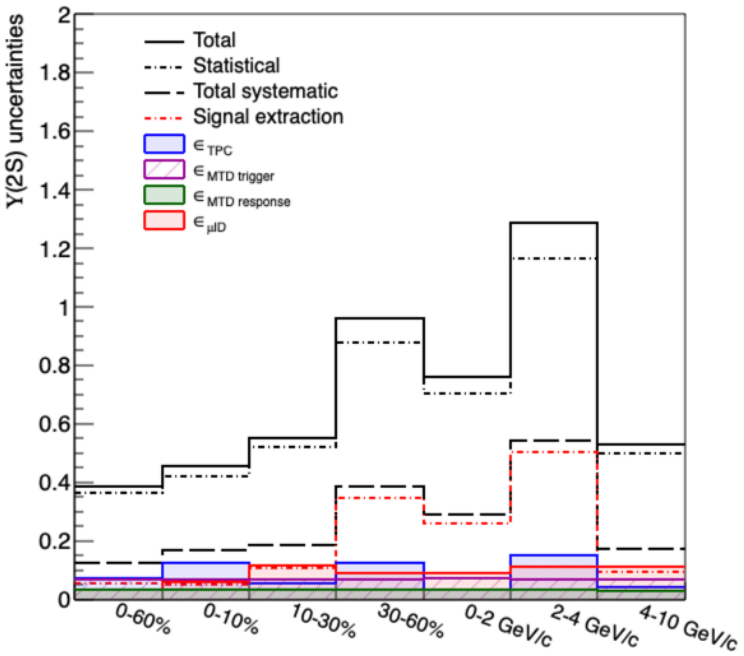

Figure 5.32: The uncertainties from different sources and the total uncertainty for Υ(2S).

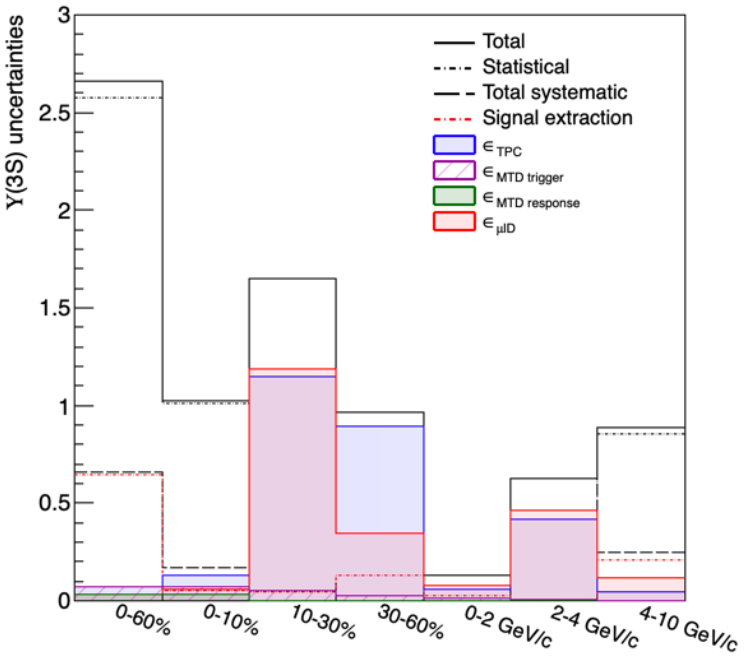

Figure 5.33: The uncertainties from different sources and the total uncertainty for Υ(3S).

	centrality & p_T bins	Stat. uncertainty	Total sys. uncertainty	Total uncertainty
	centrality: 0-60%	9.28 %	12.41 %	15.50 %
	centrality: 0-10%	14.30 %	17.67 %	22.73 %
	centrality: 10-30%	15.09 %	16.87 %	22.64 %
Υ(1S)	centrality: 30-60%	20.13 %	19.74 %	28.20 %
	$0 < p_T < 2$ GeV/c	16.32 %	14.62 %	21.91 %
	$2 < p_T < 4$ GeV/c	13.45 %	22.04 %	25.82 %
	$4 < p_T < 10$ GeV/c	24.64 %	15.67 %	29.20 %
	centrality: 0-60%	36.52 %	12.79 %	38.69 %
	centrality: 0-10%	42.30 %	16.73 %	45.49 %
	centrality: 10-30%	52.10 %	19.02 %	55.47 %
Υ(2S)	centrality: 30-60%	88.03 %	43.60 %	98.23 %
	$0 < p_T < 2$ GeV/c	70.42 %	28.11 %	75.82 %
	$2 < p_T < 4$ GeV/c	116.57 %	59.20 %	130.74 %
	$4 < p_T < 10$ GeV/c	50.00 %	16.70 %	52.71 %
	centrality: 0-60%	257.62 %	65.86 %	265.90 %
	centrality: 0-10%	100.78 %	16.94 %	102.19 %
	centrality: 10-30%	upper limit case	165.12 %	165.12 %
Υ(3S)	centrality: 30-60%	upper limit case	96.75 %	96.75 %
	$0 < p_T < 2$ GeV/c	upper limit case	13.20 %	13.20 %
	$2 < p_T < 4$ GeV/c	upper limit case	62.83 %	62.83 %
	$4 < p_T < 10$ GeV/c	85.44 %	24.58 %	88.90 %

Table 5.13: The values of the statistical, total systematic and total uncertainties in each centrality and p_T bin for Υ(1S), Υ(2S) and Υ(3S).

5.6 Results

One of the most important ingredients for Υ R_{AA} is the production cross-section of Υ in p-p collisions (pp reference). These can be obtained from Ref. [5] and the ratios of the pp reference in individual p_T bins are summarized in Table 5.14. Another key component of Υ R_{AA} is N_{coll}, and it can be found in Ref. [5]. The results in this analysis are consistent with the STAR preliminary results from the dielectron channel. The Υ(1S), Υ(2S) and Υ(3S) R_{AA} results in this analysis as a function of N_{part} and p_T are shown in Fig. 5.36 and Fig. 5.37, respectively. The detail values of Υ(1S), Υ(2S) and Υ(3S) R_{AA} in individual Υ centrality and p_T bins are summarized in Table 5.15. The red, blue, and black solid circles are the results of Υ(1S), Υ(2S) and Υ(3S) R_{AA}, respectively. The verticle bars and the open squares are the statistical and systematic uncertainties. The black arrows are the 95% C.L. upper limits for the Υ(3S) and the values are included both the statistical and the systematic uncertainties. The R_{AA} measurements for Υ(1S) and Υ(2S) of this analysis (NCKU) and the STAR preliminary results [5, 21] as a function of N_{part} and p_T are shown in Fig. 5.34 and Fig. 5.35, respectively. We also compared the R_{AA} results for Υ(1S) and Υ(2S) to several theoretical model calculations [22, 23, 24, 25]. The black solid circles are the R_{AA} results from this analysis (NCKU). The red and the blue solid stars are the STAR preliminary results from the dimuon and the dielectron channels, respectively. The verticle bars and the open squares are the statistical and systematic uncertainties. From the results in this analysis and the STAR preliminary results, the theoretical model calculations seem to be overestimated for Υ(1S) R_{AA} in almost all N_{part} and p_T bins. For the Υ(2S) R_{AA} , the results in this analysis and the STAR preliminary results are consistent with the theoretical model calculations within uncertainties. Due to the limited statistics of numbers of Υ(3S), the uncertainty of Υ(3S) R_{AA} is large. From the Υ(1S) and Υ(2S) R_{AA} results in this analysis, the R_{AA} values are lower when the Υ mesons are in the higher excited states and it is consistent with the picture of sequential melting.

	0-2 GeV/c	2-4 GeV/c	4-10 GeV/c
Υ(1S)	0.354	0.389	0.257
Υ(2S)	0.321	0.384	0.295
Υ(3S)	0.318	0.384	0.298

Table 5.14: Ratios of the pp reference in individual p_T bins for Υ(1S), Υ(2S) and Υ(3S).

	centrality & p_T bins	R_{AA}
Υ(1S)	centrality: 0-10%	$0.39 \pm 0.07 \pm 0.07$
	centrality: 10-30%	$0.29 \pm 0.04 \pm 0.05$
	centrality: 30-60%	$0.46 \pm 0.04 \pm 0.09$
	$0 < p_T < 2$ GeV/c	$0.38 \pm 0.05 \pm 0.06$
	$2 < p_T < 4$ GeV/c	$0.37 \pm 0.04 \pm 0.08$
	$4 < p_T < 10$ GeV/c	$0.34 \pm 0.07 \pm 0.05$
Υ(2S)	centrality: 0-10%	$0.26 \pm 0.09 \pm 0.04$
	centrality: 10-30%	$0.25 \pm 0.1 \pm 0.05$
	centrality: 30-60%	$0.28 \pm 0.2 \pm 0.12$
	$0 < p_T < 2$ GeV/c	$0.26 \pm 0.15 \pm 0.07$
	$2 < p_T < 4$ GeV/c	$0.1 \pm 0.09 \pm 0.06$
	$4 < p_T < 10$ GeV/c	$0.42 \pm 0.17 \pm 0.07$
Υ(3S)	centrality: 0-10%	$0.23 \pm 0.23 \pm 0.04$
	centrality: 10-30%	0.09 (upper limit case)
	centrality: 30-60%	0.31 (upper limit case)
	$0 < p_T < 2$ GeV/c	0.03 (upper limit case)
	$2 < p_T < 4$ GeV/c	0.31 (upper limit case)
	$4 < p_T < 10$ GeV/c	$0.35 \pm 0.3 \pm 0.09$

Table 5.15: The detail values of Υ(1S), Υ(2S) and Υ(3S) R_{AA} in individual Υ centrality and p_T bins. The first error is statistical and the second one is the total systematic uncertainty.

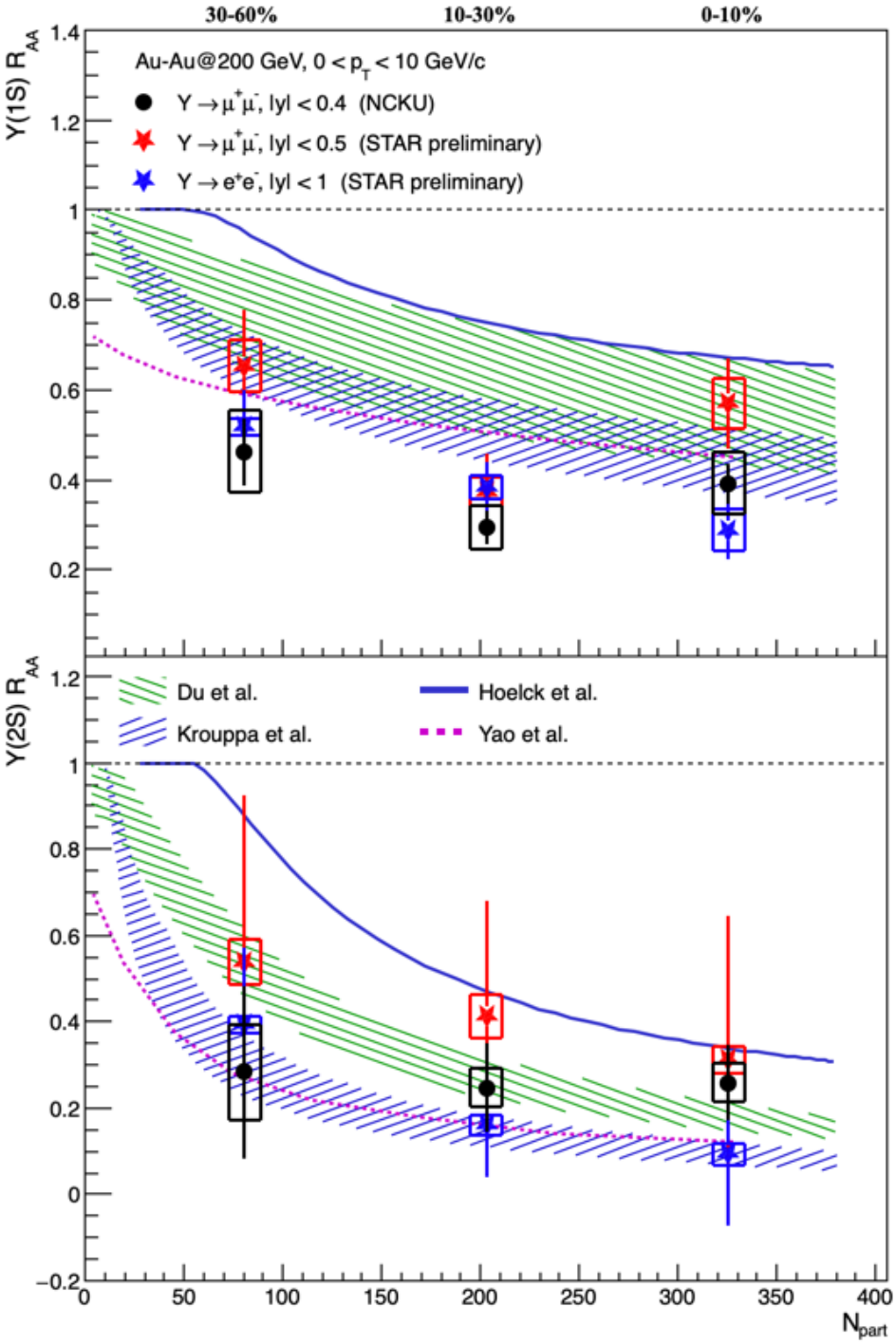

Figure 5.34: ϒ(1S) (top) and ϒ(2S) (bottom) R_{AA} as a function of N_{part} compared to the STAR preliminary results and different theoretical model calculations.

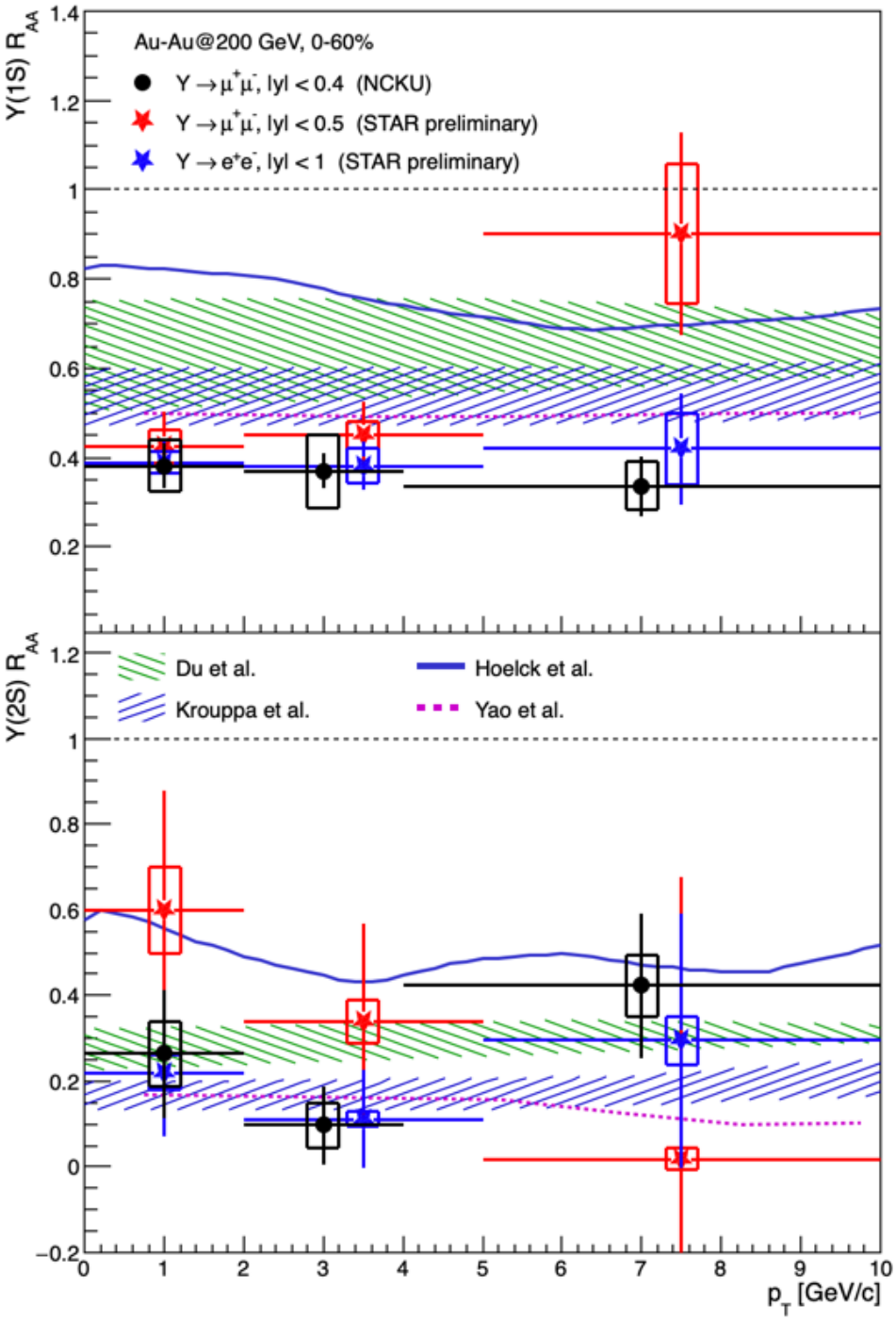

Figure 5.35: Υ(1S) (top) and Υ(2S) (bottom) R_{AA} as a function of p_T compared to the STAR preliminary results and different theoretical model calculations.

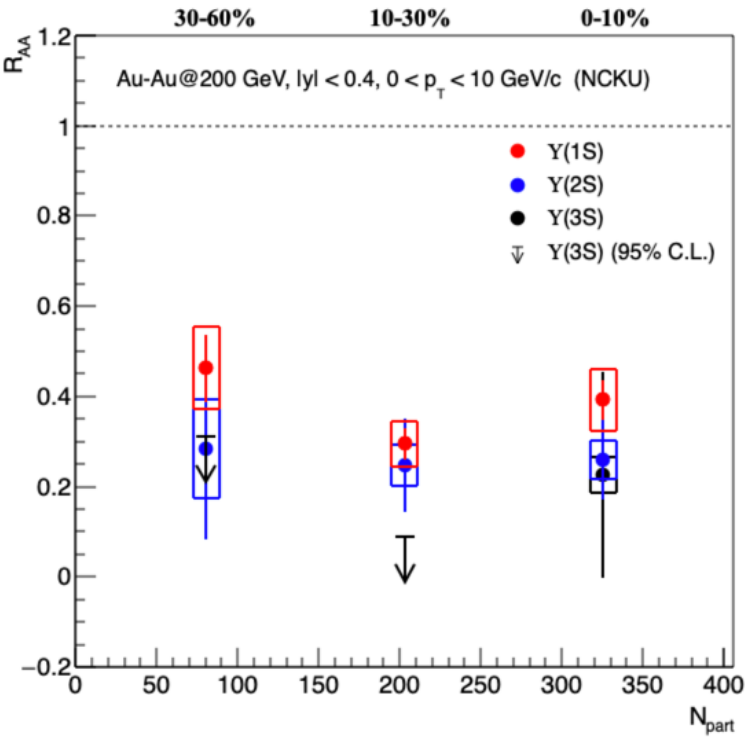

Figure 5.36: Υ(1S), Υ(2S) and Υ(3S) R_{AA} as a function of N_{part}.

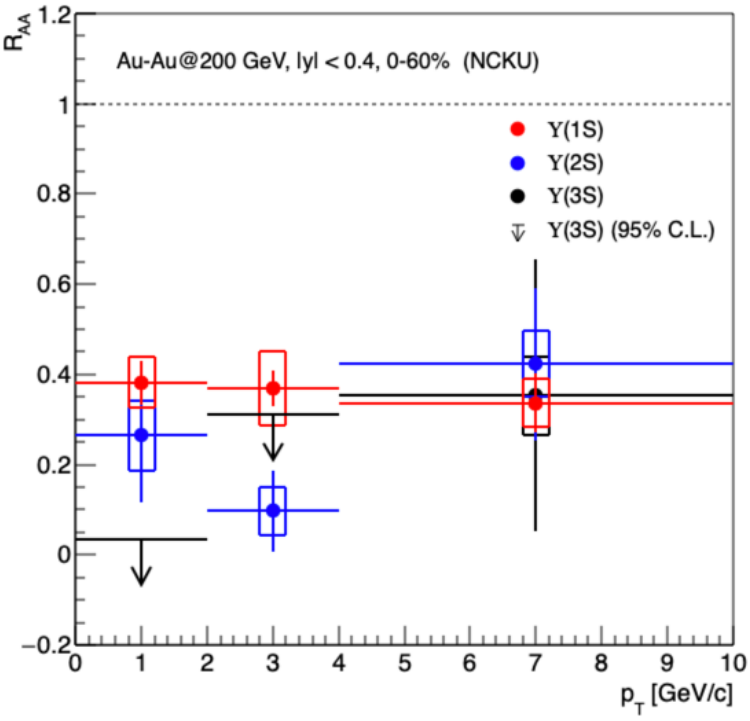

Figure 5.37: Υ(1S), Υ(2S) and Υ(3S) R_{AA} as a function of p_T.

5.7 Future work

The upper limits of the numbers of Υ(3S) in different centrality and p_T bins are estimated by the ToyMC samples in this analysis. Another method to estimate the upper limit value is the Feldman−Cousins method [26], which was used in the Run 11 Υ R_{AA} study [21] through the dielectron channel. In this method, the unbinned maximum−likelihood fit without physical limit is used in the signal extraction. The computation of the upper limit is included the total uncertainty for Υ(3S). We will also consider using the method to estimate the upper limits, and also compare with the results from other experiments to check the suppression effect for the Υ meson in different excited states and ground state.

Chapter 6 Conclusions

The analysis of the Υ suppression through the dimuon channel in Au-Au collisions at $\sqrt{s_{NN}}$ = 200 GeV uses Run 14 and Run 16 data with the corresponding luminosity of 14.2 nb^{-1} and 12.8 nb^{-1}, respectively. The MTD detector plays a critical role to enhance the purity of muon. The number of Υ used in this analysis is more than the STAR preliminary result is due to the optional p_T selection and more advanced muon identification. The measurements of Υ R_{AA} are presented in Section 5.7. The theoretical model calculations seem to be overestimated for Υ(1S) R_{AA} in almost all N_{part} and p_T bins. The results of Υ(2S) R_{AA} have good agreement with the theoretical model calculations within uncertainties. The results in this analysis are also consistent with the STAR preliminary results from the dielectron channel. From the Υ(1S) and Υ(2S) R_{AA} results, the R_{AA} values are lower for the higher Υ excited states, and this is consistent with the picture of the sequential melting of heavy quarkonia in heavy-ion collisions.

References

[1] K. A. O. et al., "Review of Particle Physics," *Chinese Physics C*, vol. 38, no. 9, p. 090001, 2014.

[2] Z. Hu and N. T. L. et al., "Review of bottomonium measurements from CMS," *International Journal of Modern Physics A*, vol. 32, 2017.

[3] V. Khachatryan and A. M. S. et al., "Upsilon Production Cross-Section in pp Collisions at $\sqrt{s_{NN}}$=7 TeV," *Physical Review D*, vol. 83, 2011.

[4] B. Mohanty, "Exploring the QCD phase diagram through high energy nuclear collisions: An overview," *PoS*, vol. CPOD2013, 2013.

[5] P. Wang, "Analysis Note: Υ measurements in Au+Au collisions at $\sqrt{s_{NN}}$ = 200 GeV via the dimuon decay channel at STAR," https://drupal.star.bnl.gov/STAR/system/files/AuAu200_Upsion_Dimuon_Ana_note_HFv1.0_0.pdf.

[6] K. H. A. et al., "STAR detector overview," *Nuclear Instruments and Methods in Physics Research Section A: Accelerators, Spectrometers, Detectors and Associated Equipment*, vol. 499, no. 2-3, pp. 624–632, 2003.

[7] S. Chatrchyan, G. Hmayakyan, and V. K. et al., "The CMS experiment at the CERN LHC," *Journal of Instrumentation*, vol. 3, 2008.

[8] M. Anderson, J. Berkovitz, W. Betts, R. Bossingham, F. Bieser, R. Brown, and M. Burks et al., "The STAR time projection chamber: a unique tool for studying high multiplicity events at RHIC," *Nuclear Instruments and Methods in Physics Research Section A: Accelerators, Spectrometers, Detectors and Associated Equipment*, vol. 499, no. 2-3, pp. 659–678, 2003.

[9] M. Williams, "Particle identification using time of flight," *Journal of Physics G: Nuclear and Particle Physics*, vol. 39, no. 12, p. 123001, 2012.

[10] L. Ruan, G. Lin, Z. Xu, K. Asselta, and H. C. et al., "Perspectives of a mid-rapidity dimuon program at the rhic: a novel and compact muon telescope detector," *Journal of Physics G: Nuclear and Particle Physics*, vol. 36, no. 9, p. 095001, 2009.

[11] R. Ma, "Analysis Note: Measurement of J/ψ suppression in Au+Au collisions at $\sqrt{s_{NN}}$ = 200 GeV through the dimuon decay channel at STAR," https://drupal.star.bnl.gov/STAR/system/files/JpsiRaa_AN.pdf.

[12] G. Aad and E. A. et al., "The ATLAS Experiment at the CERN Large Hadron Collider," *Journal of Instrumentation*, vol. 3, 2008.

[13] J. Uzan, "The big-bang theory: construction, evolution and status," *arXiv preprint astro-ph.CO/1606.06112v1*, 2016.

[14] N. B. et al., "Heavy quarkonium physics," *arXiv preprint hep-ph/0412158*, 2004.

[15] P. W. Higgs, "Broken Symmetries and the Masses of Gauge Bosons," *Physical Review L*, vol. 13, no. 16.

[16] L. M. L. et al., "The Upsilon Particle," *Scientific American*, vol. 239, no. 4, pp. 72–84, 1978.

[17] I. Lakomov, "Mesure de la production de J/ψ en collisions p-Pb au LHC avec le spectromètre à muons d' ALICE," *Ph.D. dissertation*, 2014.

[18] M.Krämer, "Quarkonium production at high-energy colliders," *arXiv preprint hep-ph/0106120*, 2001.

[19] T. Huang, R. Ma, B. Huang, X. Huang, L. Ruan, T. Todoroki, Z. Xu, C. Yang, S. Yang, Q. Yang, Y. Yang, and W. Zha, "Muon identification with muon telescope detector at the star experiment," *Nuclear Instruments and Methods in Physics Research Section A: Accelerators, Spectrometers, Detectors and Associated Equipment*, vol. 833.

[20] J. Adam, L. Adamczyk, J. R. Adams, J. K. Adkins, G. Agakishiev, M. M. Aggarwal, Z. Ahammed, I. Alekseev, D. M. Anderson, and R. A. et al., "Measurements of the transverse-momentum-dependent cross sections of J/ψ production at mid-rapidity in proton + proton collisions at $\sqrt{s_{NN}}$ = 510 and 500 gev with the star detector," *Physical Review D*, vol. 100.

[21] S. Yang, "Analysis Note: Observation of squetial Upsilon ($\Upsilon \to e^+e^-$) suppression in Au+Au collisions at $\sqrt{s_{NN}}$ = 200 GeV with STAR experiment," https://www.star.bnl.gov/protected/heavy/syang/run11/anaNote/upsilonAN_v2.pdf.

[22] X. Du and M. H. et al., "Color screening and regeneration of bottomonia in high-energy heavy-ion collisions," *Physical Review C*, vol. 96, p. 054901, 2017.

[23] B. Krouppa and A. R. et al., "Bottomonium suppression using a lattice QCD vetted potential," *Physical Review D*, vol. 97, p. 016017, 2018.

[24] J. Hoelck and F. N. et al., "In-medium Υ suppression and feed-down in UU and PbPb collisions," *Physical Review C*, vol. 95, p. 024905, 2017.

[25] X. Y. et al., "Quarkonium production in heavy ion collisions: coupled Boltzmann transport equations," *Nuclear Physics A*, vol. 982, pp. 755–758, 2019.

[26] G. J. Feldman and R. D. Cousins, "Unified approach to the classical statistical analysis of small signals," *Physical Review D*, vol. 57, no. 7, p. 3873, 1998.